NATIONAL ADVISORY COMMITTEE FOR AERONAUTICS

TECHNICAL NOTE 4092

EXPERIMENTAL DROPLET IMPINGEMENT ON FOUR BODIES OF REVOLUTION

By James P. Lewis and Robert S. Ruggeri

Lewis Flight Propulsion Laboratory
Cleveland, Ohio

Washington
December 1957

NATIONAL ADVISORY COMMITTEE FOR AERONAUTICS

TECHNICAL NOTE 4092

EXPERIMENTAL DROPLET IMPINGEMENT ON FOUR BODIES OF REVOLUTION

By James P. Lewis and Robert S. Ruggeri

SUMMARY

The rate and area of cloud droplet impingement on four bodies of revolution were obtained experimentally in the NACA Lewis icing tunnel with a dye-tracer technique. The study included spheres, ellipsoidal forebodies of fineness ratios of 2.5 and 3.0, and a conical forebody of 30° included angle and covered a range of angles of attack from 0° to 6° and rotational speeds up to 1200 rpm. The data were obtained at an airspeed of 157 knots and are correlated by dimensionless impingement parameters.

In general, the experimental data show that the local and total impingement rates and impingement limits of bodies of revolution are primarily functions of the modified inertia parameters, the body shape, and fineness ratio. Both the local impingement rate and impingement limits depend upon the angle of attack. Rotation of the bodies had a negligible effect on the impingement characteristics except for an averaging effect at angle of attack. For comparable diameters the bluffer bodies had the largest total impingement efficiency, but the finer and sharper bodies had the largest values of maximum local impingement efficiency and, in most cases, the largest limits of impingement. In most cases, the impingement characteristics were less than those calculated from theoretical trajectories; in general, however, fairly good agreement was obtained between the experimental and theoretical impingement characteristics.

INTRODUCTION

The design and evaluation of icing protection equipment for aircraft components require a knowledge of the local and total rates of cloud droplet impingement and the surface extent of droplet impingement. These impingement characteristics are important in determining the extent of a surface requiring icing protection, the local and total protection requirements, the shape, size, and location of ice formations on aircraft components, and the aerodynamic penalties associated with icing of aircraft surfaces.

Previous studies (refs. 1 to 7) have reported the impingement characteristics of various two- and three-dimensional bodies. The impingement characteristics of bodies of revolution are of interest because such bodies are representative of many aircraft components subject to icing such as radomes, body noses, engine accessory housings, and the large spinners of turboprop engines. Most of the previous investigations of cloud droplet impingement on bodies of revolution (refs. 2 to 7) have been either analytical computations or were experimental studies of limited scope. In particular, little experimental information is available on the effects of angle of attack and rotation on impingement characteristics.

As part of a general study of icing and icing protection of bodies of revolution, an experimental investigation of the impingement characteristics of four bodies of revolution was conducted in the Lewis icing tunnel using the NACA dye-tracer technique (ref. 8). The object of the investigation was to obtain sufficient experimental data to enable the impingement characteristics to be determined over a range of body shapes and operating and meteorological conditions including angle of attack and rotation.

The bodies studied included spheres, ellipsoidal forebodies, and a conical forebody. The impingement characteristics were obtained for volume-median droplet diameters ranging from 11.5 to 18.6 microns, angles of attack of 0°, 3°, and 6°, rotational speeds of 0, 600, 800, and 1200 rpm, and a nominal airspeed of 157 knots. The experimental results are presented in terms of dimensionless impingement parameters and are compared with theoretically calculated impingement characteristics.

APPARATUS

The study of droplet impingement on bodies of revolution was made in the 6- by 9-foot test section of the Lewis icing tunnel using the NACA dye-tracer technique. In this technique (ref. 8) water containing known small amounts of a water-soluble dye is sprayed into the tunnel airstream a large distance ahead of the test body. The surface of the body is covered with absorbent blotting paper upon which the dyed-water droplets impinge. The amount of dye trace deposited in a measured time interval can be converted into the amount of water impinging at any particular location by a colorimetric analysis. If the spray-cloud water content and droplet size are known, the impingement characteristics of the body can be readily determined.

The test bodies used included two spheres of 5.92- and 18-inch diameters, two ellipsoidal forebodies of 2.5 and 3.0 fineness ratios (minor axes of 30 and 20 in., respectively), and a conical forebody of 30° included angle (base diameter, 18.93 in.). The ellipsoidal and conical forebodies were mounted on a faired afterbody of 30-inch maximum diameter

as shown in figure 1. This afterbody, containing the drive motor for rotation and instrumentation pickups, was the same as that used in reference 9. The spheres were sting-mounted.

In order to obtain the correct droplet trajectories in the tunnel, the droplets must be traveling parallel to and at the same speed as the free airstream after passing through the tunnel contraction section and before being subjected to the test-body flow field. The distances from the nose of the models to the tunnel test-section entrance are given in the following table in terms of the body maximum radius. Also given in the table are the minimum dimensionless distances ahead of the model as computed in references 2 and 4 that are required to obtain essentially undisturbed free-stream conditions.

Body	Dimensionless distance ahead of model, x/R	
	Experimental, from model nose to test-section entrance	Theoretical, required for free-stream conditions
Spheres		
5.92-In. diam.	53	14 (ref. 4)
18-In. diam.	16.5	14 (ref. 4)
Ellipsoids		
2.5:1	7.8	--
3.0:1	12.5	--
5:1	----	15 (ref. 2)
Conical	12.0	--

The ellipsoidal and conical models were fabricated of 0.062-inch-thick aluminum spun to the desired shape with a transition section fairing the contour between the rear of the test body and the afterbody. Both sphere models were made of laminated mahogany. Sketches of the models showing the pertinent dimensions and details including the orientation of the blotting-paper strips are presented in figure 2. Both elliptical forebodies were halves of exact ellipsoids. The conical body, however, had an apex foreshortened $1\frac{1}{2}$ inch which resulted in a nose rounded to a 1/2-inch radius. The surface of the conical model was slightly convex and deviated from a true cone by a maximum of approximately 0.6 inch. The surfaces of all the models were smooth and free from irregularities with the exception of the conical body which had some waviness (sensitive to touch) at a circumferential weld about halfway between the nose and the base.

Pressure distributions over the model surfaces for the conical and ellipsoidal forebodies were obtained by means of pressure belts cemented to the model surface for the stationary case and by flush static taps and a rotating pressure pickup for the rotating case.

The spray cloud was provided by nine air-water atomizing nozzles located in the quieting chamber upstream of the tunnel test section. The nozzles were positioned to supply a cloud of uniform liquid-water content of the required droplet size in the tunnel test section. The spray was turned on and off by fast-acting solenoid valves, and the spray duration was set and recorded by an electric timer. Further details of the spray system are given in reference 8.

PROCEDURE

The experimental procedure was, in general, the same as that described in references 1 and 8. Strips of the blotter paper were attached to the model, and, then, with the tunnel air properly conditioned as to speed, temperature, and humidity, the spray, preloaded to the desired air and water pressures, was turned on for the preset time interval. The blotter was then removed from the model for the colorimetric analysis.

The blotters were narrow strips, 3/4 and 1 inch wide, which were cemented to vellum strips which in turn were cemented to the model surface. The edges of the blotters were taped to the model surface. Cementing and taping prevented lifting of the blotter from the model surface and also prevented damage to the blotter during removal. The orientation of the blotters was as shown in figure 2. A continuous strip was wrapped around the model in a horizontal plane over the 0° and 180° meridian stations. For the stationary model a second blotter strip was attached at the 90° meridian station which was butted against the first strip at the model base.

The investigation reported herein was conducted at an airstream velocity of 157 knots, a static pressure of 28 inches of mercury, and a static air temperature of 50° F. Data were obtained at angles of attack of 0°, 3°, and 6° and at rotational speeds of 0, 600, 800, and 1200 rpm. The variations in angle of attack and rotational speeds were chosen as being representative of current and near-future aircraft. The droplet sizes used in the study were as follows:

Water-air mass-flow ratio	Volume-median droplet diameter, d_{med}, microns	Maximum droplet diameter, $d_{med,max}$, microns
0.34	11.5	24
.49	14.7	35
.61	16.7	45
.76	18.6	64.5

The droplet-size distribution is given in figure 3. The volume-median droplet size and size distribution were determined by the Joukowski-aspirator method discussed in reference 1. For each water-air mass-flow ratio, a relatively uniform cloud with local liquid-water-content variations within ±10 percent and essentially the same droplet-size distribution was obtained. The reproducibility of the average liquid-water content and volume-median diameter was within approximately ±6 percent. For most cases a repeat run was made at each set of conditions.

ANALYSIS OF DATA

The analysis of the data obtained from the dye-impinged blotters gives the local and total impingement efficiencies and the surface extent of impingement. The method of analysis used herein is essentially that presented and described in detail in reference 8 with modifications required for use with bodies of revolution. The local water impingement rate was determined by colorimetric analysis wherein small circular segments, 3/8 inch in diameter, were punched from the exposed blotter strip at specified locations. The dye was dissolved out of the segment with a known quantity of distilled water, and the concentration of dye in this solution was determined by a calibrated colorimeter. With the exposure time and the original concentration of dye in the spray cloud known, the local impingement rate per unit area was obtained by the relation

$$\overline{W}_\beta = \frac{0.794\ Pb}{tc\ \Delta A_s},\ \text{(lb water)/(hr)(sq ft)} \tag{1}$$

(All sybmols are defined in the appendix.)

The local impingement efficiency $\overline{\beta}$ can be obtained by the equation

$$\overline{\beta} = \frac{\overline{W}_\beta}{0.225\ U_0 w_t} \tag{2}$$

The total impingement efficiency $\overline{E}_m$ is obtained by integrating $\overline{\beta}$ over the surface area impinged and dividing by a reference area. Thus,

$$\overline{E}_m = \frac{1}{A_f}\int_{A_s=0}^{A_s=\max}\ \frac{1}{2\pi}\int_{\theta=0}^{\theta=2\pi}(\overline{\beta}\ d\theta)dA_s \tag{3}$$

or, in terms of the surface distance from the nose and body radius,

$$\bar{E}_m = \frac{1}{\pi R^2} \int_{s=0}^{s_{max}} \int_{\theta=0}^{\theta=2\pi} (\bar{\beta}\, d\theta) r\, ds \qquad (4)$$

For zero angle of attack stationary, an arithmetic average of the $\bar{\beta}$ value at the three meridional stations was used. For rotation the measured $\bar{\beta}$ values were averages of the circumferential variation. For these two cases the integration was performed in the axial direction only. By definition the total impingement efficiency $\bar{E}_m$ is the ratio of the total amount of water impinging on the body to the maximum amount that could impinge (straight-line droplet trajectories). Therefore, the term A_f in equation (3) should be the maximum projected frontal area of the body. For angle of attack this area is not the maximum cross-sectional area of the body. For the range of angles of attack and body sizes and shapes investigated, the difference between the projected area and the maximum cross-sectional area was very small (less than 5 percent at 6° angle of attack). The maximum cross-sectional area πR^2 was used, as indicated in equation (4), for purposes of convenience in the results reported herein.

The impingement characteristics $\bar{\beta}$, $\bar{E}_m$, and $(s/R)_{max}$ are presented in terms of the dimensionless parameters K, Φ, and Re_0. The K and Φ parameters are defined in terms of the maximum radius of the body R. The inertia and free-stream Reynolds number parameters are normally defined in terms of the volume-median droplet diameter (K_{med} and $Re_{0,med}$) except when they are used to correlate the limit of impingement, in which case the maximum droplet diameter is used (K_{max} and $Re_{0,max}$). The parameter K is indicative of the inertia of the droplet, and Φ represents the deviation of drag forces from Stokes' law. Impingement characteristics are also presented as a function of the modified inertia parameters $K_{0,med}$ and $K_{0,max}$ to obtain a correlation independent of Φ. This modified inertia parameter is defined as

$$K_0 = K(\lambda/\lambda_s)$$

where λ/λ_s (the range ratio) is given as a function of Re_0 in figure 4. This variation may be approximated within 10 percent for the normal range of Re_0 ($25 < Re_0 < 1000$). By using this relation K_0 is related to airspeed, droplet diameter, body size, and air properties. Thus,

$$K_0 = 3.86\times10^{-10}\left(\frac{U_0}{\mu}\right)^{0.6} \frac{d^{1.6}}{\rho^{0.4}R} \qquad (5)$$

The values of K_0 used herein were computed by using figure 4 rather than equation (5).

RESULTS

Velocity Distribution

The measured surface velocity distributions are presented and compared with theoretical values in order to indicate any differences between the actual flow field and the theoretical flow field and, hence, possible reasons for deviations that may exist between the experimental and theoretically calculated impingement characteristics. In addition, comparison of the effects of changes in the operating variables (angle of attack, body shape, and rotational speed) on the experimental velocity distributions indicate the changes in the flow fields. Such comparisons are helpful, therefore, in evaluating the effects of the operating variables on impingement characteristics for cases in which theoretically predicted values of impingement characteristics are either limited or lacking. All the data presented are uncorrected for tunnel wall effects.

Spheres. - The experimental local velocity distribution for the 18-inch-diameter sphere is presented in figure 5. The experimental values agree well with theory up to an s/R value of approximately 1.4 (central angle, 80°). Although no measurements were made on the 5.92-inch-diameter sphere, it is expected that the velocity distribution would be similar to that shown in figure 5 because the Reynolds numbers of both spheres (8.1×10^6 and 24.5×10^6) were considerably greater than the critical Reynolds number of 10^5.

Ellipsoids. - The local velocity distribution for the stationary ellipsoidal forebodies of fineness ratios of 2.5 and 3.0 is presented in figure 6. For both bodies the experimental values agree well with theoretical predictions obtained by the method of reference 10. As would be expected, these blunt body shapes caused only small changes in the flow around the bodies when the angle of attack was increased from 0° to a maximum of 6°. Practically no variation of the velocity ratio with Reynolds number was obtained over the range investigated $\left(2.6\times10^6 < \frac{U_0 \rho D}{\mu} < 5.8\times10^6\right)$.

For rotation the true local velocity with respect to the model surface was not measured because the local total pressure was not obtained. However, measurements of the local surface static pressure (corrected for centrifugal force) during rotation were essentially the same as those obtained stationary. The local velocity while rotating was computed therefore as the resultant of the rotational component and the stationary longitudinal component. The maximum resultant velocities (at largest body radius and 1200 rpm) computed in this manner were only 6 percent larger than the velocity while stationary for the 3.0:1 ellipsoid and 11 percent larger for the 2.5:1 ellipsoid.

Conical forebody. - The velocity distribution for the conical body (fig. 7) showed a peak followed by a reversal near the nose for all conditions investigated. This velocity peak and reversal occurred at the region where the spherical nose became tangent to the conical surface. Included in figure 7 is the theoretical velocity distribution for a true cone of 15° half-angle at zero angle of attack which differed from the experimental distribution by a maximum of 9 percent in the region of reversing velocity. However, the velocity distributions over the spherical nose cap ($s/R < 0.05$) agreed well with the theoretical distribution over the front of spheres. Angles of attack up to 6° changed the local velocities by less than 10 percent and caused no change in the location of the velocity peak. The local velocities with respect to the body surface during rotation were obtained in the same manner as for the ellipsoidal bodies. The resultant of the rotating component and the stationary longitudinal component gave values 6 percent larger than the velocity obtained stationary.

Local Impingement Characteristics

The experimental impingement results are presented first in the form of the local impingement efficiency $\bar{\beta}$ for the specific operating and cloud droplet conditions. Later the experimental results are correlated with the modified inertia parameter K_0. Comparisons are also made with values computed from theoretical impingement relations wherein the theoretical values are weighted to the tunnel droplet-size distribution. The results for the several different bodies are discussed separately.

Spheres. - The local impingement efficiency as a function of the dimensionless surface distance from the nose (sphere stagnation point) is presented in figures 8 and 9 for the 5.92- and 18-inch-diameter spheres, respectively. The data show the expected increase in local impingement efficiency with increasing volume-median droplet size and the inverse relation with increasing body diameter. The multiple points plotted at several surface distance locations were obtained from repeat runs (tailed symbols) and from diametrically opposite sides of the body for the same run. These data for the sphere are typical of all the impingement data reported herein in regard to the degree of repeatability and the magnitude of scatter. The experimental data gave a reasonably well defined value of impingement efficiency at stagnation. At the limit of impingement, however, the asymptotic shape of the impingement curve made experimental determination of the extent of impingement rather inexact.

The theoretical local impingement efficiency obtained from the impingement relations of reference 4 and weighted to the tunnel droplet-size distribution is also shown in figures 8 and 9 for each volume-median droplet size. In general, fairly good agreement was obtained between the

experimental and theoretical results, particularly with respect to the shape of the curve of local impingement variation over the sphere. At the smallest volume-median droplet size the theoretical values exceed the experimental impingement efficiencies; as the droplet size is increased, the experimental values approach and in some cases exceed the theoretical. These discrepancies between the theoretical and experimental results may be attributed to experimental inaccuracy in the measurement of the rate of water impingement, the accuracy of the theoretical calculations, the validity of the assumptions made in the development of the theoretical equations, and the accuracy of the experimental values of droplet size, size distribution, and water content. The known variation in the measured value of the volume-median droplet size (±6 percent) would be sufficient to account for most of the differences between the experimental and theoretical values.

Ellipsoids. - The variation of the local impingement efficiency over the body surface is shown in figure 10 for two stationary ellipsoids at zero angle of attack. Data obtained at the 0°, 90°, and 180° meridional locations are presented for four volume-median droplet sizes. The data scatter and reproducibility as well as the general trends of increasing impingement efficiency with increasing volume-median droplet size are similar to those obtained with the spheres.

In order to show the effect of body shape on the local impingement efficiency, comparisons between the sphere and ellipsoids should be made on the basis of equal body and droplet size since both of these factors are known to change impingement efficiency. Such comparisons can be made from the data of figures 8, 9, and 10 if equal values of the modified inertia parameter are used, as is shown in the section Correlation of Impingement Characteristics and in reference 1. A comparison of the local impingement efficiency on the sphere ($K_{0,med}$ = 0.09, 14.7 microns, fig. 9(b)) with that for the 2.5:1 ellipsoid ($K_{0,med}$ = 0.08, 18.6 microns, fig. 10(a)) shows considerable differences. The general curvature of the β curve for the sphere is much less than for the ellipsoid. The greatest difference between the two bodies, however, is found at stagnation where the local impingement efficiency for the ellipsoid is approximately twice that for the sphere. Similar results are obtained comparing the 3.0:1 ellipsoid and sphere. By comparing the 2.5:1 (18.6 microns, fig. 10(a)) and 3.0:1 (14.7 microns, fig. 10(b)) ellipsoids at $K_{0,med}$ = 0.08 the effects of the small change in fineness ratio upon the local impingement efficiency are seen to be relatively minor. At the nose the impingement efficiencies of the two bodies are very nearly the same, while on the rest of the body the blunter body (2.5:1) has a slightly greater impingement efficiency.

A comparison of the experimental local impingement efficiency for the 3.0:1 fineness ratio ellipsoid at zero angle of attack with the theoretical

values of reference 7 is shown in figure 11 for four volume-median droplet diameters. The experimental values agree fairly well with the computed results at the largest volume-median droplet diameter (18.6 microns), but the comparison becomes increasingly poorer as the droplet size decreases. The theoretical curves differ from the experimental both in magnitude and curvature. This is especially true at the stagnation point and at the aft portion of the impinged area.

The local impingement efficiency values obtained on the two stationary ellipsoids at angles of attack of 3° and 6° are presented in figure 12 for three meridional locations. Included are faired curves of the local impingement efficiency obtained at zero angle of attack. In general, the effects of angle are as might be expected from the variation of local velocity distribution with angle of attack (fig. 6). The values of impingement efficiencies and limits of impingement are increased on the windward (0°) meridian while those on the leeward side (180°) are reduced. The shapes of the curves, however, are changed little as the effect of angle primarily shifts the curves to the windward side. A slight change in the location of the maximum $\bar{\beta}$ was obtained, and the peak $\bar{\beta}$ value was located between the air stagnation point and the foremost point of the body. This effect was greatest at an angle of attack of 6° and on the ellipsoid of a fineness ratio of 2.5. Changes in the magnitude of the maximum $\bar{\beta}$ were obtained at angle of attack, but significant trends cannot be determined because of the limitations of the experimental data. The $\bar{\beta}$ values for the 90° meridian (solid symbols) fall between those on the 0° and 180° meridans.

The peripheral distribution of the local impingement efficiency is shown better in figure 13 which presents cross plots of the data of figure 12. Results are given for the two ellipsoids at an angle of attack of 6° for the largest and smallest volume-median droplet sizes. Values obtained at zero angle of attack are included for comparison. The peripheral distribution of impingement is very similar for both ellipsoids. The greatest peripheral variation for both ellipsoids occurred at distances from the nose s/R of approximately 0.2 to 0.4.

The effect of body rotation upon the local impingement efficiency of ellipsoids is shown in figure 14 for several volume-median droplet sizes, angles of attack, and rotational speeds. Included in figure 14 for comparative purposes are the envelopes of the data spread obtained with the stationary bodies at zero angle of attack. Although in some cases there are slight indications of an increase in impingement efficiency with rotation, in general the effect of rotation appeared to be negligible up to 1200 rpm. This result agrees with that obtained for the velocity distribution where the effects of rotation were also negligible. No significant trends in the data obtained during body rotation were found with respect to angle of attack, droplet size, or body geometry.

Conical forebody. - The experimental values of local impingement efficiency obtained on the stationary conical forebody at zero angle of attack are presented in figure 15 for three volume-median droplet diameters. These results are all characterized by a rapid decrease of $\bar{\beta}$ within a region approximately 1 inch from the nose, followed by a rather extensive region of relatively low values of $\bar{\beta}$. The junction between the two portions of the $\bar{\beta}$ curve occurs near the surface location at which the hemispherical nose cap becomes tangent to the conical surface. Compared to the sphere and ellipsoids the extent of impingement is fairly extensive. For the smallest volume-median droplet size (11.5 microns) the limit of impingement (approx. 18 in.) is about one-half the total surface distance of the conical forebody as compared with approximately one-sixth (5 in.) for the 3.0:1 ellipsoid.

A comparison of the experimental local impingement efficiency on the stationary conical forebody with theoretical values at zero angle of attack for three volume-median droplet sizes is presented in figure 16. For the purpose of the theoretical comparison a hypothetical body was assumed to be made up of a true cone of 15° half-angle and a spherical nose of 1-inch diameter. The theoretical impingement for the spherical nose was obtained from calculated data for spheres of reference 4 and for the cone proper from the data of reference 7. Faired values of the experimental $\bar{\beta}$ are presented on the left of figure 16 while on the ordinates to the right an arithmetic average of the experimental results is plotted to an expanded abscissa as step values averaged over the area of 3/8-inch-diameter punch used in the dye analysis. The agreement between the experimental and theoretical results in general is considered fairly good. Over the spherical nose cap the experimental values are consistently less than those predicted for a true sphere. On the conical body proper the experimental and theoretical values, while of the same order of magnitude, cross each other at surface distances of approximately 7 to 10 inches from the nose with the theoretical limit of impingement considerably larger than that obtained experimentally. The differences between the experimental and theoretical values on the cone proper are believed to result primarily from the convexity of the test body surface, while at the nose the lack of agreement is partially attributed to the presence of the conical body behind the small spherical segment.

The experimental impingement obtained on the stationary conical body for the leeward and windward meridans at angles of attack of 3° and 6° is presented in figures 17(a) and (b), respectively. Results for the 90° meridian are also shown in figure 17(b) (solid symbols). The effect of angle of attack is similar to that obtained for the ellipsoidal body, that is, an increase of local impingement efficiency and limit of impingement on the windward meridian and a decrease on the leeward meridian. A comparison of the effect of angle of attack is given in figure 17(c) for a volume-median droplet diameter of 18.6 microns. The maximum value of $\bar{\beta}$ on the spherical nose segment showed only negligible variation with angle

of attack. At an angle of attack of 6° and the smallest volume-median droplet size the impingement on the leeward meridian extended only about 1 inch from the nose (fig. 17(b)). However, for the largest volume-median droplet size at the same angle of attack, impingement occurred over practically the entire windward side. The peripheral variation of local impingement efficiency on the conical forebody at an angle of attack of 6° is illustrated in figure 18 for two volume-median droplet diameters. The general trends of peripheral distribution are similar to those obtained on the ellipsoidal forebody but with a more extreme variation, especially in the nose region.

The effect of rotation on the local impingement efficiency of the conical forebody was negligible for all conditions investigated. A comparison of the impingement efficiency obtained at 1200 rpm for several angles of attack and volume-median droplet sizes with the values obtained for the stationary body at zero angle of attack is presented in figure 19.

Correlation of Impingement Characteristics

The prime impingement characteristics $\bar{E}_m$ and $(s/R)_{max}$ are correlated with the modified inertia parameters $K_{0,med}$ and $K_{0,max}$, respectively, in order to compare and readily extrapolate the experimental and calculated results.

Spheres. - The experimental total impingement efficiency $\bar{E}_m$ for spheres is presented in terms of $K_{0,med}$ in figure 20. The theoretical results of reference 4 are also given for two values of the independent impingement parameter Φ (one for each sphere radius). The separation of the curves for the two Φ values indicates the degree with which the K_0 correlation eliminates the effect of the Φ parameter. Theoretical curves are given for both a uniform droplet diameter and for the tunnel droplet-size distribution which is essentially a Langmuir "D" distribution (ref. 11). Both the correlation of the experimental data and the comparison with the theoretical curve (weighted to the tunnel droplet-size distribution) are considered fairly good. Although the experimental data for each body size appear to cross the theoretical curve, the accuracy of the experimental data is such as to preclude the determination of such systematic trends. The known accuracy of the volume-median droplet diameter yields a variation of $K_{0,med}$ of approximately ±10 percent which would account for most of the scatter of the data from the theoretical "D" curve. The theoretical curve for the uniform droplet diameter is given to show the magnitude of the effect of droplet-size distribution on $\bar{E}_m$ and not to suggest the presence of a uniform-droplet-diameter cloud in the tunnel tests. Plotting $\bar{\beta}_{max}$ against $K_{0,med}$ would give a correlation similar to that obtained for $\bar{E}_m$. Correlation of the limit of

impingement on spheres with the modified inertia parameter based upon the maximum droplet size $K_{0,max}$ is presented in figure 21. The same general trends were obtained as for $\bar{E}_m$.

Ellipsoids. - The correlation of the total impingement efficiency with $K_{0,med}$ for the two ellipsoidal bodies shown in figure 22 has the same trends as obtained with the sphere. The experimental results in most cases are lower than the theoretical values especially for the smallest volume-median droplet sizes. As was indicated by the local impingement efficiency, rotation had no significant effect on $\bar{E}_m$. The data obtained at an angle of attack of 6° indicated a slight increase in total impingement efficiency over that obtained at zero angle of attack although the effect is of the same order of magnitude as the data scatter. The data also tended to confirm the theoretically predicted increase in total impingement efficiency with decrease in fineness ratio for bodies of the same maximum diameter.

The limit of impingement as a function of the modified inertia parameter based upon the maximum droplet size $K_{0,max}$ is presented in figure 23. Although the experimental data correlate fairly well with $K_{0,max}$ there is a considerable lack of agreement with the theoretical values, particularly with respect to the predicted effect of fineness ratio. However, both the limits of impingement and the maximum droplet diameter are difficult to determine. The effects of angle of attack are consistent for both bodies and fairly well defined. At an angle of attack of 6° the impingement on the windward meridian is as much as twice that at zero angle of attack, while for the leeward meridian only a relatively slight decrease in the limit of impingement was obtained at 6°.

Conical forebody. - The correlation of total impingement efficiency with the modified inertia parameter $K_{0,med}$ for the conical forebody is shown in figure 24 for several operating and droplet-size conditions. Included for comparison are theoretical total impingement efficiencies on a true cone of 15° half-angle taken from reference 7. Theoretical curves are given for both the tunnel droplet-size distribution (approximately a Langmuir "D" distribution) and for a uniform droplet diameter distribution. The experimental values of $\bar{E}_m$ for the conical forebody are the lowest of all the bodies tested. Operation at angle of attack or with rotation had only negligible effects on the total collection efficiency, and no systematic trends were obtained. The differences between the theoretical values and the exerimental data are believed to result in large part from the difference in body shape between the conical forebody model and a true cone.

The correlation of the limit of impingement on the conical forebody with modified inertia parameter $K_{0,max}$ is shown in figure 25. Although

the exact limits of impingement were difficult to measure, the trends shown by the data of figure 25 are believed to be valid. At zero angle of attack the experimental limit of impingement shows a considerable increase with increasing $K_{0,max}$ as compared with the essentially uniform value of a true cone. The smaller limits of impingement obtained experimentally compared with the theoretical values result primarily from the convexity of the surface of the test body compared to a true cone. Operation at angle of attack with a stationary body resulted in wide ranges of limit of impingement varying from a value slightly greater than the nose-cap extent on the leeward meridian for the smallest droplet size to practically the rear of the body on the windward meridian for the largest droplet size. The decrease in limit of impingement on the windward meridian at an angle of attack of 3° compared with zero angle of attack is questionable and may result from surface irregularities and convexity. Rotation of the body had the effect only of distributing the extent of impingement evenly over the body surface at a value corresponding to that obtained on the windward meridian stationary at the corresponding angle of attack.

CONCLUDING REMARKS

The impingement characteristics of the several bodies of revolution have been discussed separately. A comparison of the impingement on the different bodies to show the effects of body shape and fineness ratio can be made in several ways. The method adopted herein compares plots of the local impingement efficiency as a function of the dimensionless surface area from the body nose A_s/A_f for specified values of $K_{0,med}$. In many practical cases the distribution of impingement as a function of surface area is of greater importance than in terms of axial or surface distance. Comparing on the basis of a constant $K_{0,med}$ is the same, of course, as exposing various bodies of the same maximum diameter to droplets of the same diameter at the same free-stream velocity, air temperature, and pressure conditions. Comparisons of the local impingement efficiency on a sphere, the 3.0:1 ellipsoid, and the conical forebody are made in figure 26 for three values of the inertia parameter at zero angle of attack. The $\bar{\beta}$ values of figures 26(a) and (b) are experimental results, while for $K = \infty$ (straight-line droplet trajectories) $\bar{\beta}$ is the value of local body slope. Included in figure 26(c) is $\bar{\beta}$ for a true 15° half-angle cone. The area under the curves is the total impingement efficiency, $\bar{E}_m$ by definition. A comparison of the $\bar{\beta}$ profiles over the K range shows in general the same relation; the sphere has the most gradual change over the impinged area, while the conical body has a steep gradient and a distinct knee in the curve close to the body nose. Except for $K = \infty$ the conical forebody has the largest values of $\bar{\beta}_{max}$ and the sphere the least. The ellipsoid had the largest limit of impingement except at the smallest value of $K_{0,med}$. The sphere, however, has the greatest total impingement

efficiency and the conical body the least, with the ellipsoid in between. In general, both the experimental and theoretical results indicate that, for bodies of the same diameter, the bluff bodies have the largest total impingement efficiency while the finer bodies have the largest values of $\bar{\beta}_{max}$ and $(s/R)_{max}$.

The experimental impingement characteristics, in general, show a degree of correlation with the modified inertia parameter (in which airspeed and droplet and body sizes are the most significant variables) that is satisfactory for engineering design purposes. Additional factors affecting the impingement characteristics are body shape, fineness ratio, and angle of attack. Both the local impingement rate and limit of impingement depend upon angle of attack, but the total impingement rate is rather insensitive to angles of attack up to 6°. Rotation of the bodies investigated had only a negligible effect on the impingement characteristics except for an averaging effect at angle of attack.

The experimental impingement results presented herein are considered in general to show agreement with theoretical values ranging from satisfactory to good, with the best agreement occurring where the theoretical data are well defined over the range of tunnel test conditions. The presence of the afterbody is believed to have only a minor effect on the experimental results since the experimental velocity distributions agreed well with the theoretical values for the ellipsoidal bodies. This indicates an adequate simulation of the flow field. In addition, the 2.5:1 ellipsoid which had the same maximum diameter as the afterbody and the spheres which were sting-mounted showed approximately the same degree of scatter and agreement with theory as did the 3.0:1 ellipsoid. All the experimental data showed a tendency to be slightly lower than the theoretically predicted values. A similar trend was obtained in reference 1. The best agreement of the experimental impingement characteristics with theoretical values was obtained for the spheres and ellipsoidal bodies. Full agreement with the theoretical results of reference 7 for the conical forebody was precluded because the geometry of the experimental body differed from that of a true cone.

The conclusions of reference 1 apply with regard to application of the experimental impingement data to flight or design conditions. That is, the tunnel droplet-size distribution is typical of that found in many natural icing situations, and the droplet sizes and liquid-water contents measured in flight by rotating multicylinders can be related to the value quoted for the tunnel (Joukowski-aspirator method) by the data of figure 19 of reference 1. In addition, it is felt that the correlation of the impingement characteristics with the modified inertia parameter, the range of variables covered by the experimental investigation, the degree of agreement with theoretical results, and the rather extensive computed impingement characteristics of references 2, 3, 4, and 7 permit accurate

determination of the impingement characteristics of various bodies of revolution over the practical combination of meteorological and operating conditions.

Lewis Flight Propulsion Laboratory
National Advisory Committee for Aeronautics
Cleveland, Ohio, July 23, 1957

APPENDIX - SYMBOLS

A area, sq ft

b volume of distilled water used to dissolve dye from blotter segments, ml

c percent concentration by weight of dye in water solution used in spray system, (lb dye/lb solution) $\times 100$ percent $\approx$ (lb dye/lb water) $\times 100$ percent

D body maximum diameter, ft

d droplet diameter, microns (3.28×10^{-6} ft)

E_m total impingement efficiency defined by eqs. (3) and (4), dimensionless

K inertia parameter, $(3.28 \times 10^{-6} d)^2 \frac{U_0 \rho d}{18 \mu R} = 1.16 \times 10^{-12} \frac{d^2 U_0}{\mu R}$, dimensionless

K_0 modified inertia parameter, $(\lambda / \lambda_s) K$, dimensionless

P concentration of solution obtained from blotter segments, mg dye/ml solution

R body maximum radius or semiminor axis, ft

Re_0 free-stream Reynolds number with respect to droplet, $\frac{3.28 \times 10^{-6} d \rho U_0}{\mu} = \sqrt{K \Phi}$, dimensionless

r local body radius, ft

s surface distance referenced to body nose, ft

t exposure time, sec

U_0 free-stream velocity, ft/sec or knots $\times 1.689$

U_1 local velocity at outer edge of boundary layer, ft/sec or knots $\times 1.689$

W_β local impingement rate in cloud of uniform droplet size, lb/(hr)(sq ft)

w_t total liquid water content of cloud, $\bar{g}$/cu m

x axial distance referenced to body nose, ft

α body angle of attack, deg

β local impingement efficiency in cloud of uniform droplet size, defined by eq. (2), dimensionless

θ meridional angle, deg

λ true range of droplet as projectile injected into still air, ft

λ_s range of droplet as a projectile following Stokes' law, ft

μ viscosity of air, (lb/sec)/sq ft

ρ density of air, slugs/cu ft

ρ_d density of droplet, 1.94 slugs/cu ft

Φ independent impingement parameter, $\frac{18\rho^2 RU_0}{\mu\rho_d} = 9.28\,\frac{\rho^2 RU_0}{\mu}$, dimensionless

Subscripts:

f frontal projected

max maximum

med volume median

s surface

0 free stream

1 boundary-layer outer edge

Superscripts:

$\bar{}$ weighted value resulting from effects of more than one droplet size

REFERENCES

1. Gelder, Thomas F., Smyers, William H., Jr., and von Glahn, Uwe: Experimental Droplet Impingement on Several Two-Dimensional Airfoils with Thickness Ratios of 6 to 16 Percent. NACA TN 3839, 1956.

2. Dorsch, Robert G., Brun, Rinaldo J., and Gregg, John L.: Impingement of Water Droplets on an Ellipsoid with Fineness Ratio 5 in Axisymmetric Flow. NACA TN 3099, 1954.

3. Brun, Rinaldo J., and Dorsch, Robert G.: Impingement of Water Droplets on an Ellipsoid with Fineness Ratio 10 in Axisymmetric Flow. NACA TN 3147, 1954.

4. Dorsch, Robert G., Saper, Paul G., and Kadow, Charles F.: Impingement of Water Droplets on a Sphere. NACA TN 3587, 1955.

5. Lewis, James P., and Blade, Robert J.: Experimental Investigation of Radome Icing and Icing Protection. NACA RM E52J31, 1953.

6. Lenherr, F. E., and Young, R. W.: Computation of Water Catch on Axial Symmetric Aircraft Radomes. TDM-77, Northrop Aircraft, Inc., Dec. 17, 1952. (Prog. Rep. III, Contract AF 33(038)-1817.)

7. Torgeson, W. L., and Abramson, A. E.: A Study of Heat Requirements for Anti-Icing Radome Shapes with Dry and Wet Surfaces. WADC Tech. Rep. 53-284, Wright Air Dev. Center, Wright-Patterson Air Force Base, Sept. 1953. (Contract AF 33(616)-85, RDO No. 664-802.)

8. von Glahn, Uwe H., Gelder, Thomas F., and Smyers, William H., Jr.: A Dye-Tracer Technique for Experimentally Obtaining Impingement Characteristics of Arbitrary Bodies and a Method for Determining Droplet Size Distribution. NACA TN 3338, 1955.

9. Lewis, James P., and Ruggeri, Robert S.: Investigation of Heat Transfer from a Stationary and Rotating Ellipsoidal Forebody of Fineness Ratio 3. NACA TN 3837, 1956.

10. Zahm, A. F.: Flow and Drag Formulas for Simple Quadrics. NACA Rep. 253, 1927.

11. Langmuir, Irving, and Blodgett, Katherine B.: A Mathematical Investigation of Water Droplet Trajectories. Tech. Rep. No. 5418, Air Materiel Command, AAF, Feb. 19, 1946. (Contract No. W-33-038-ac-9151 with General Electric Co.)

(a) Ellipsoidal forebody of fineness ratio of 3.0 (20-in. diam.).

Figure 1. - Installation of bodies of revolution in icing tunnel.

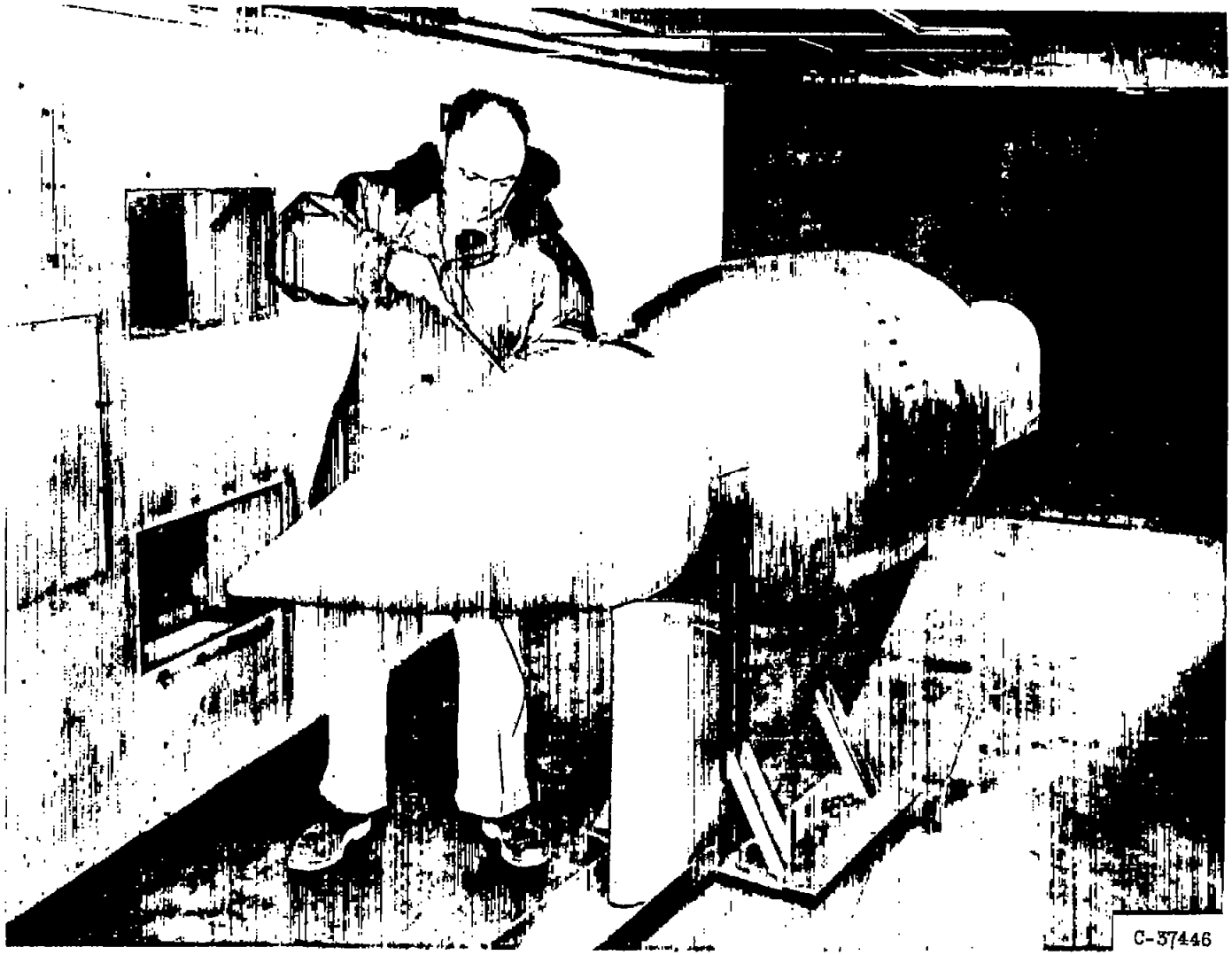

(b) Conical forebody (18.93-in. base diam.).

Figure 1. - Concluded. Installation of bodies of revolutions in icing tunnel.

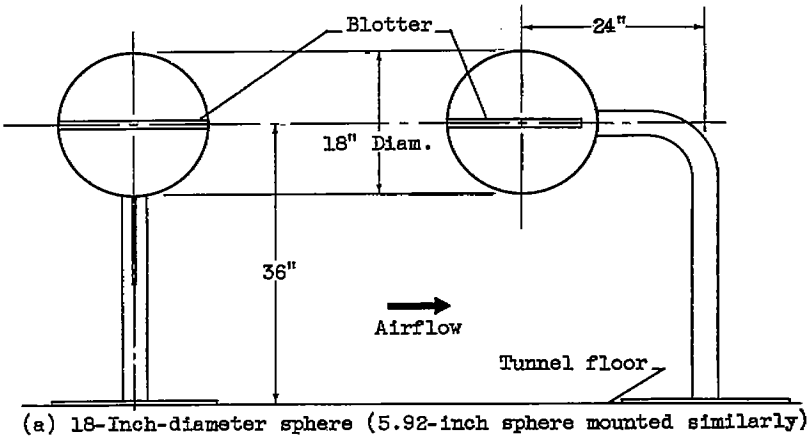

(a) 18-Inch-diameter sphere (5.92-inch sphere mounted similarly).

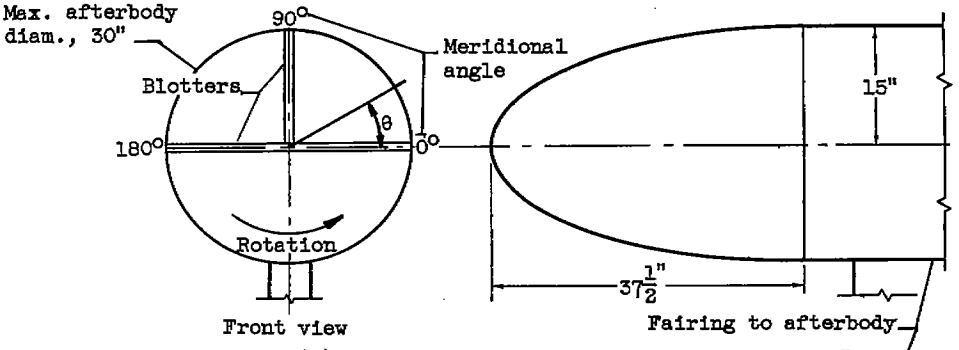

(b) Ellipsoidal forebody; fineness ratio, 2.5.

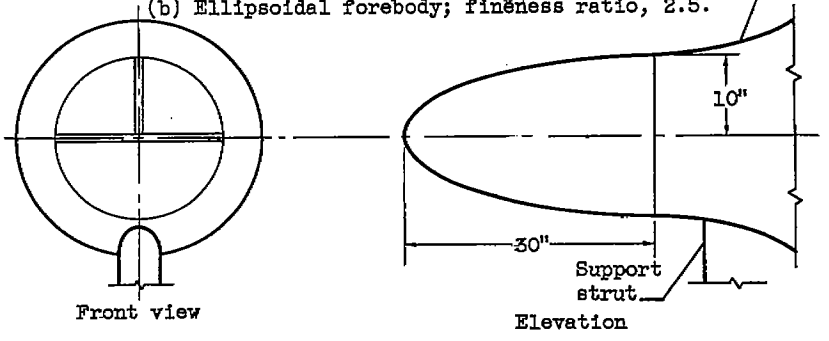

(c) Ellipsoidal forebody; fineness ratio, 3.0.

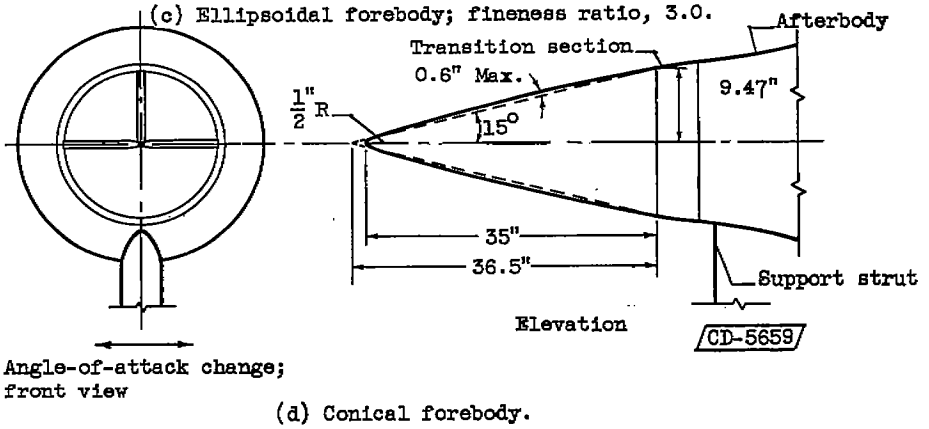

(d) Conical forebody.

Figure 2. - Schematic views of impingement test bodies of revolution.

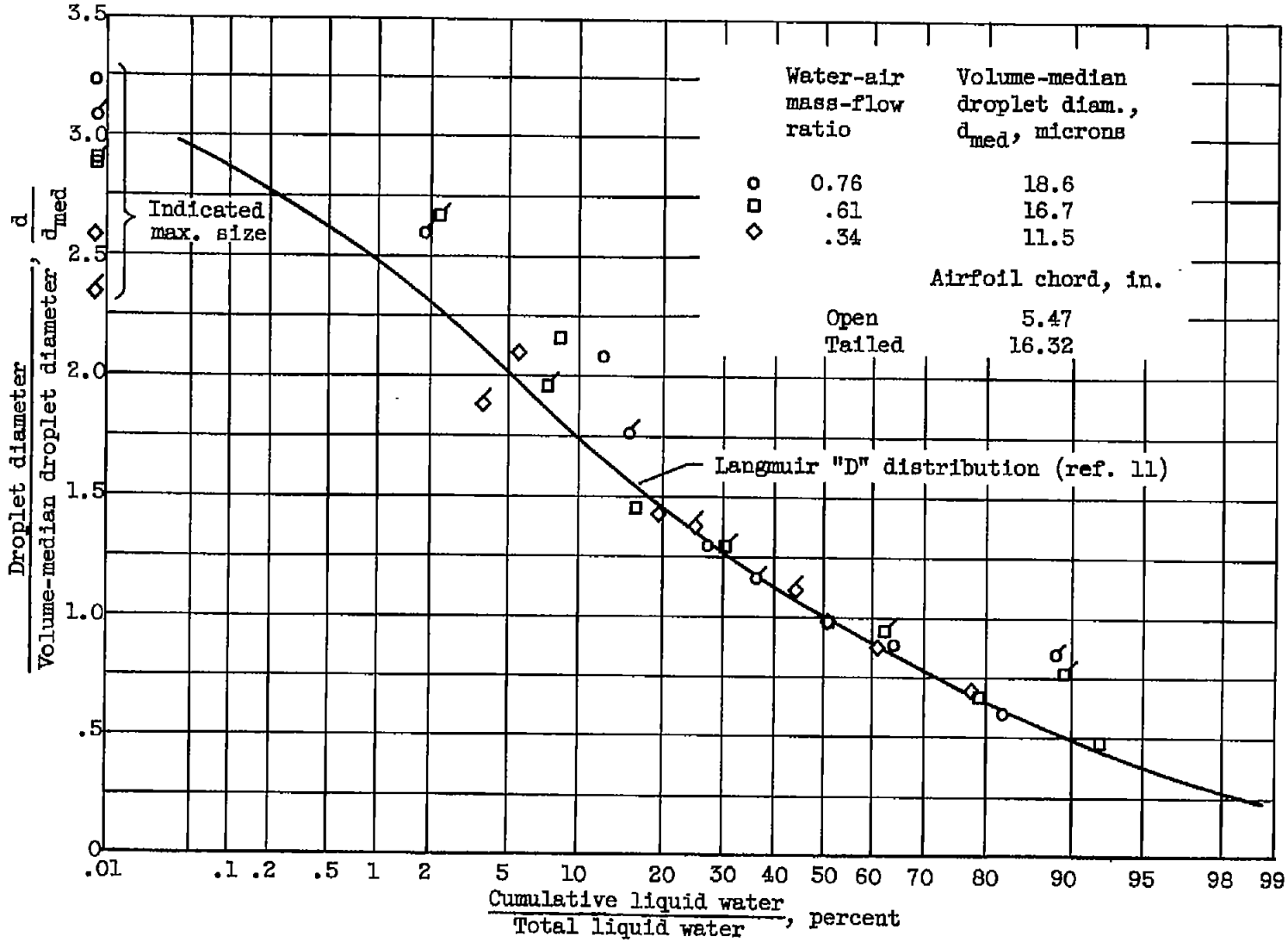

Figure 3. - Dimensionless droplet-size distribution of tunnel spray obtained on 36.5-percent Joukowski airfoil (ref. 1).

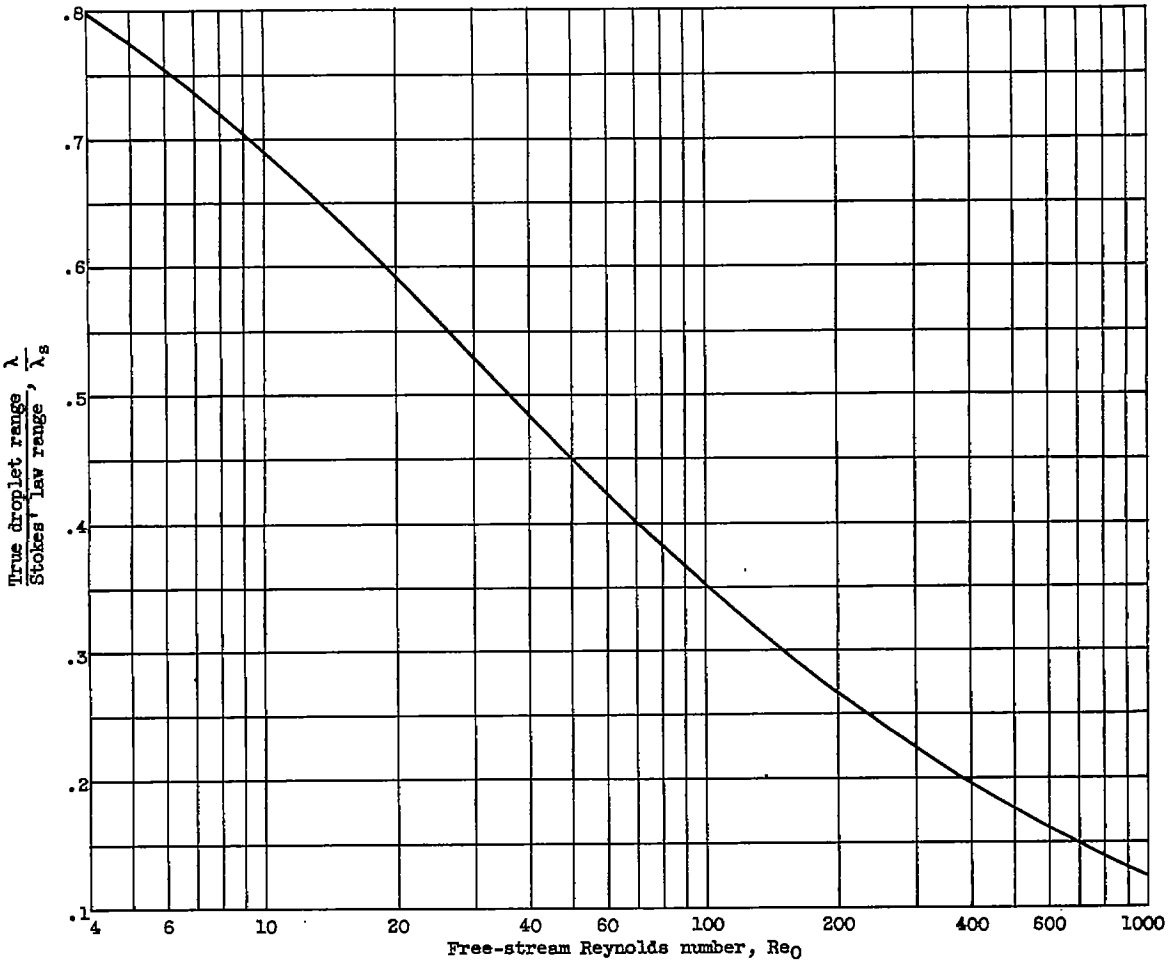

Figure 4. - Droplet range ratio as function of droplet Reynolds number (data from ref. 11).

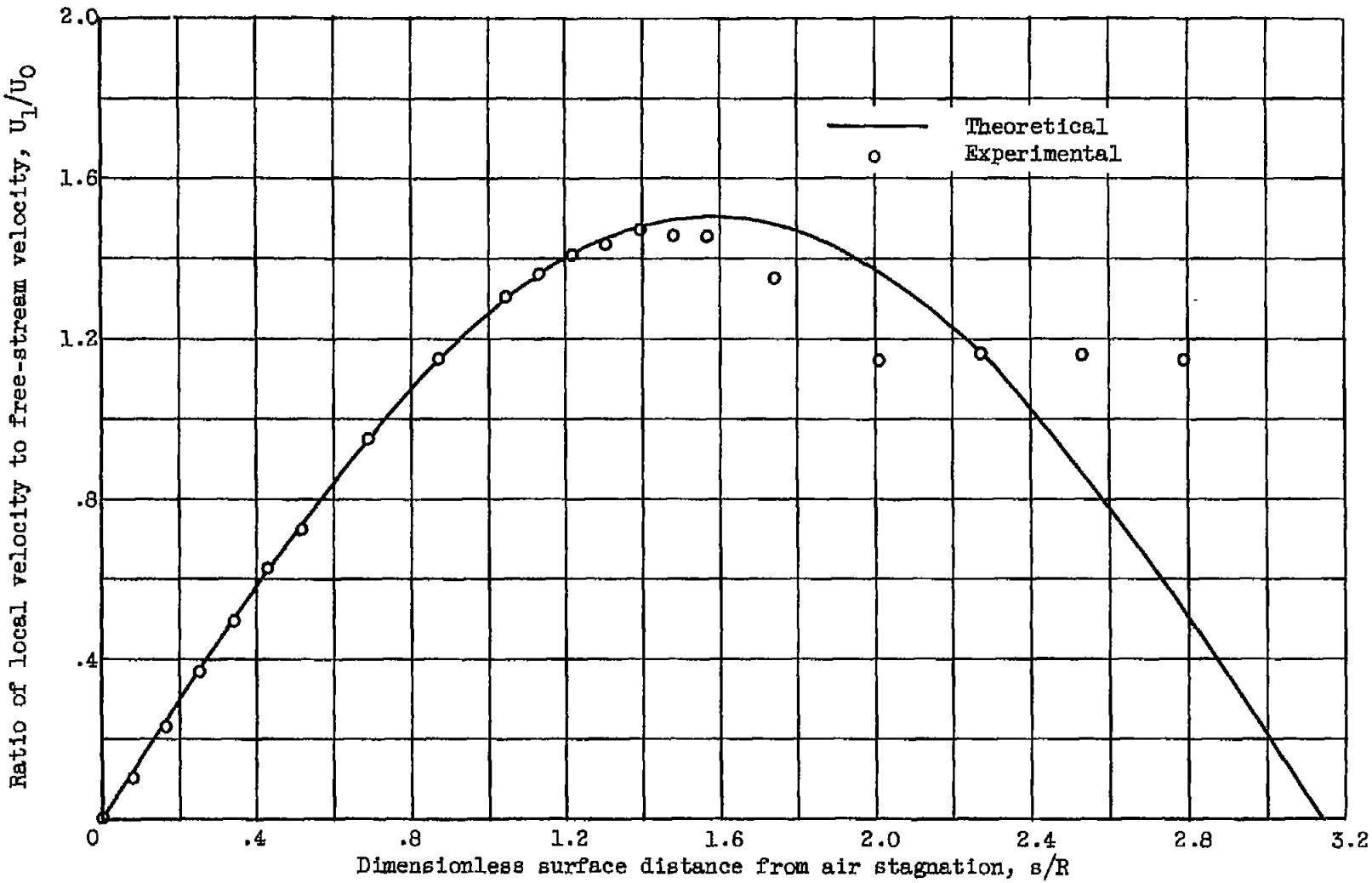

Figure 5. - Velocity distribution over 18-inch-diameter sphere.

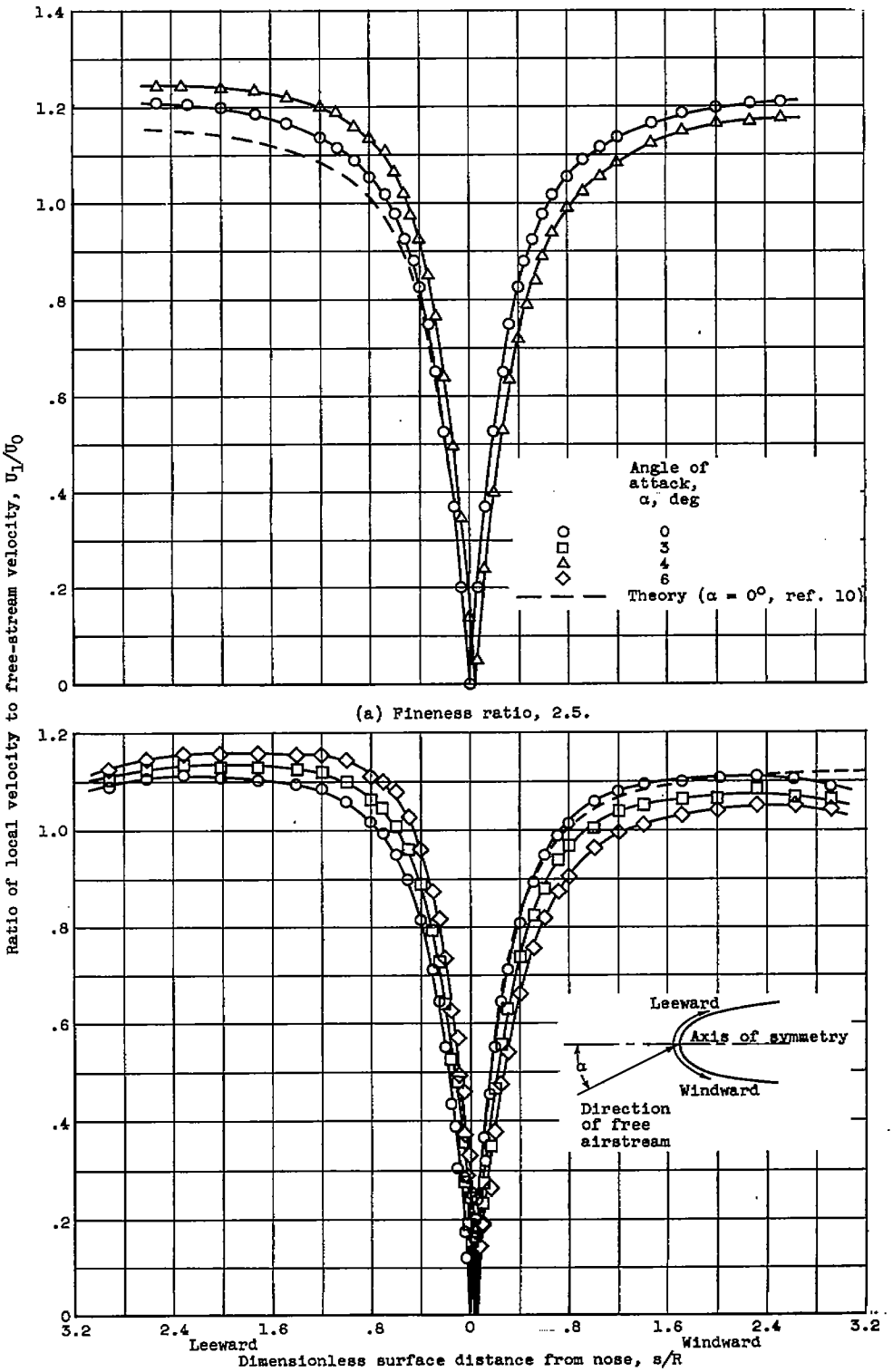

Figure 6. - Velocity distribution over stationary ellipsoidal forebodies.

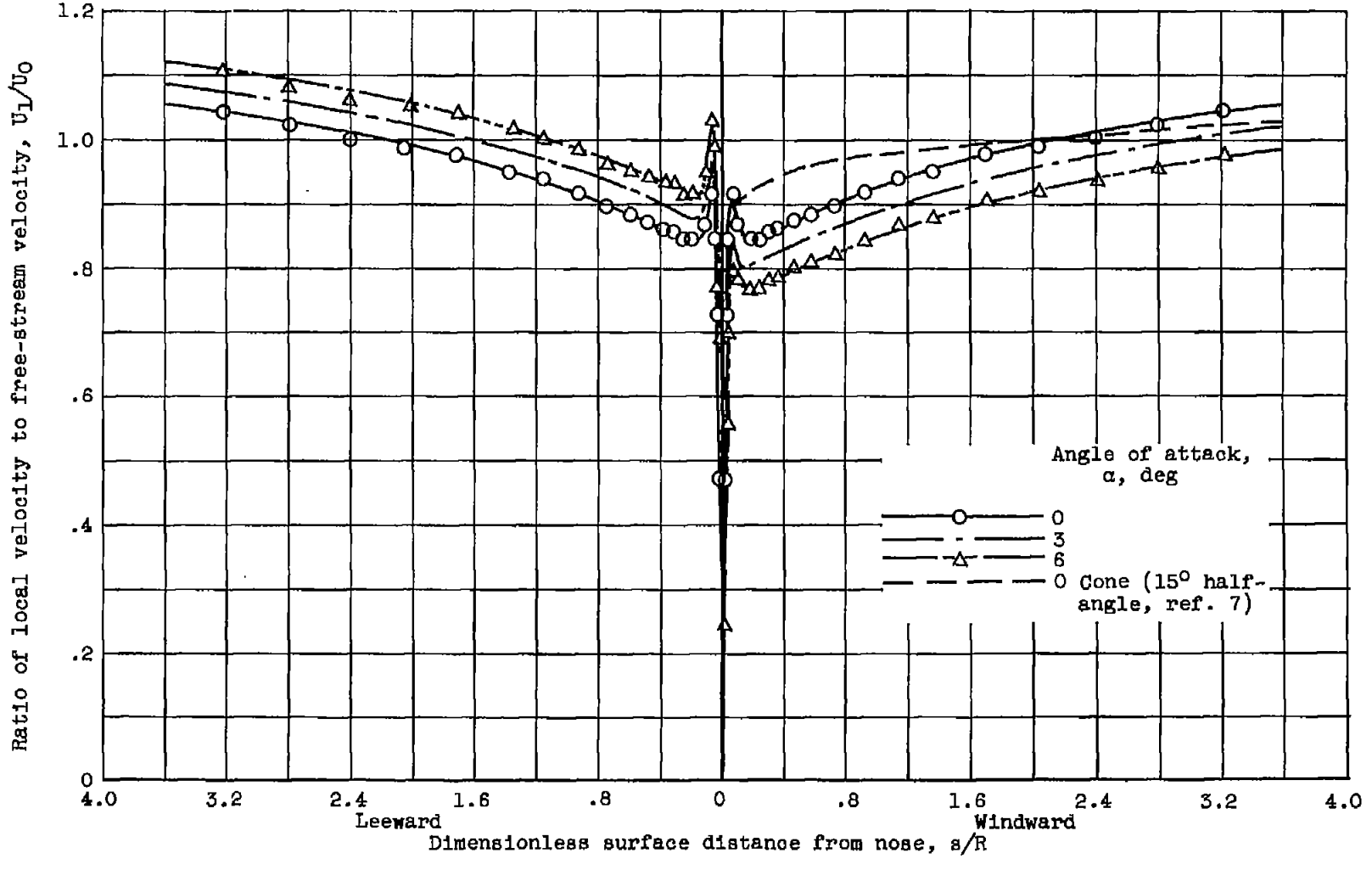

Figure 7. - Velocity distribution over a stationary conical forebody at three angles of attack.

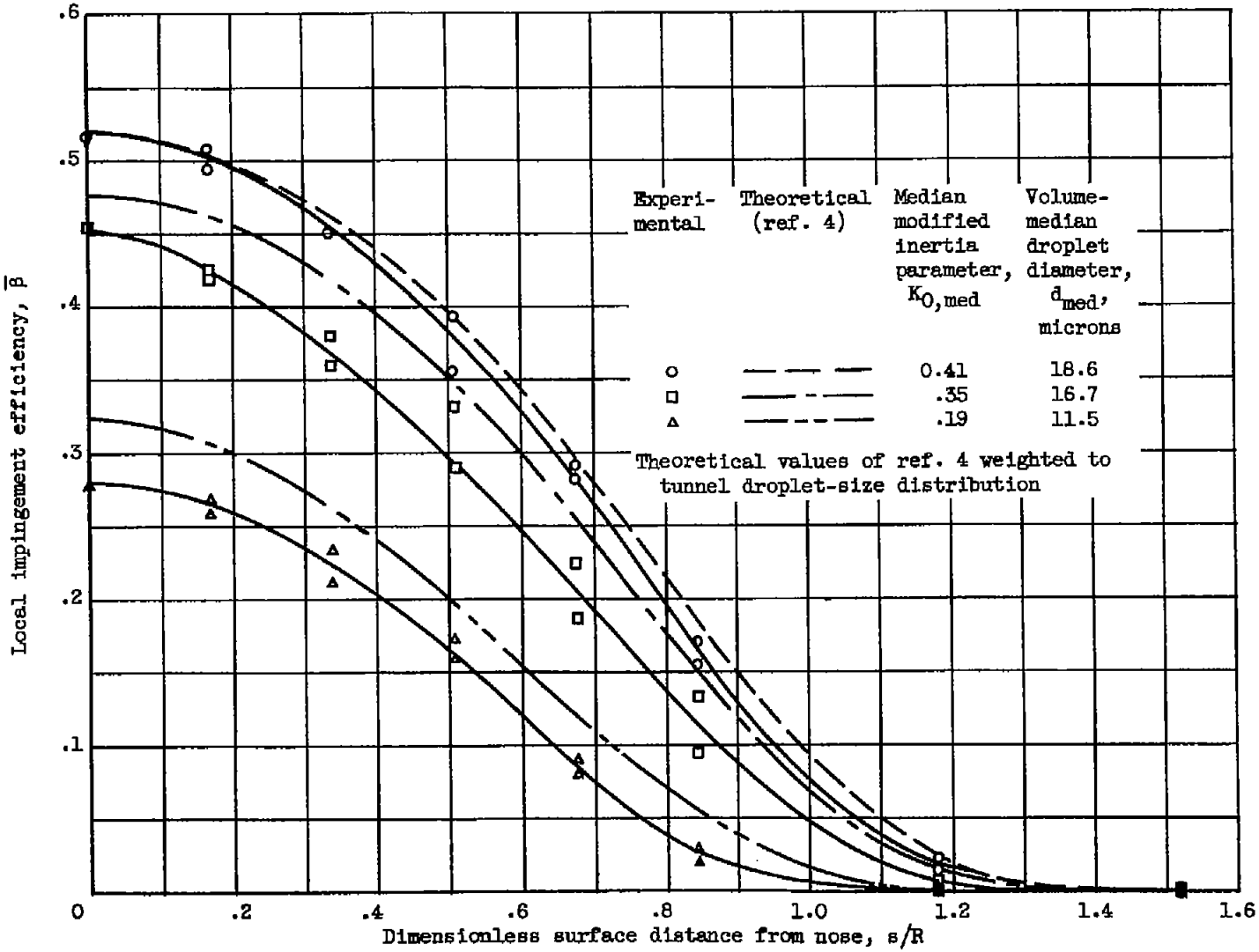

Figure 8. - Comparison of experimental and theoretical local impingement efficiencies for 5.92-inch-diameter sphere at three droplet diameters.

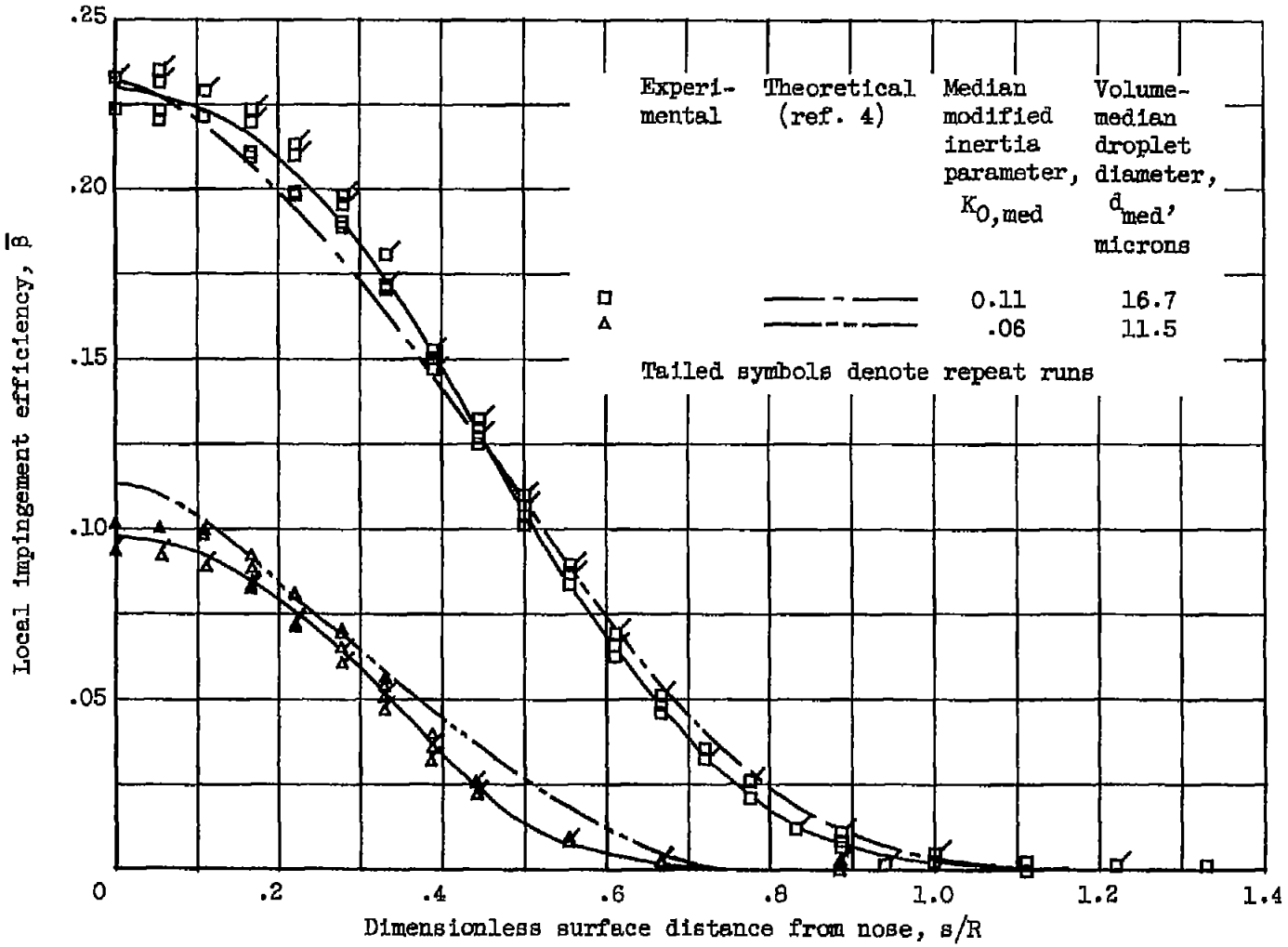

(a) Droplet diameters, 16.7 and 11.5 microns.

Figure 9. - Comparison of experimental and theoretical local impingement efficiencies for 18-inch-diameter sphere at four droplet diameters.

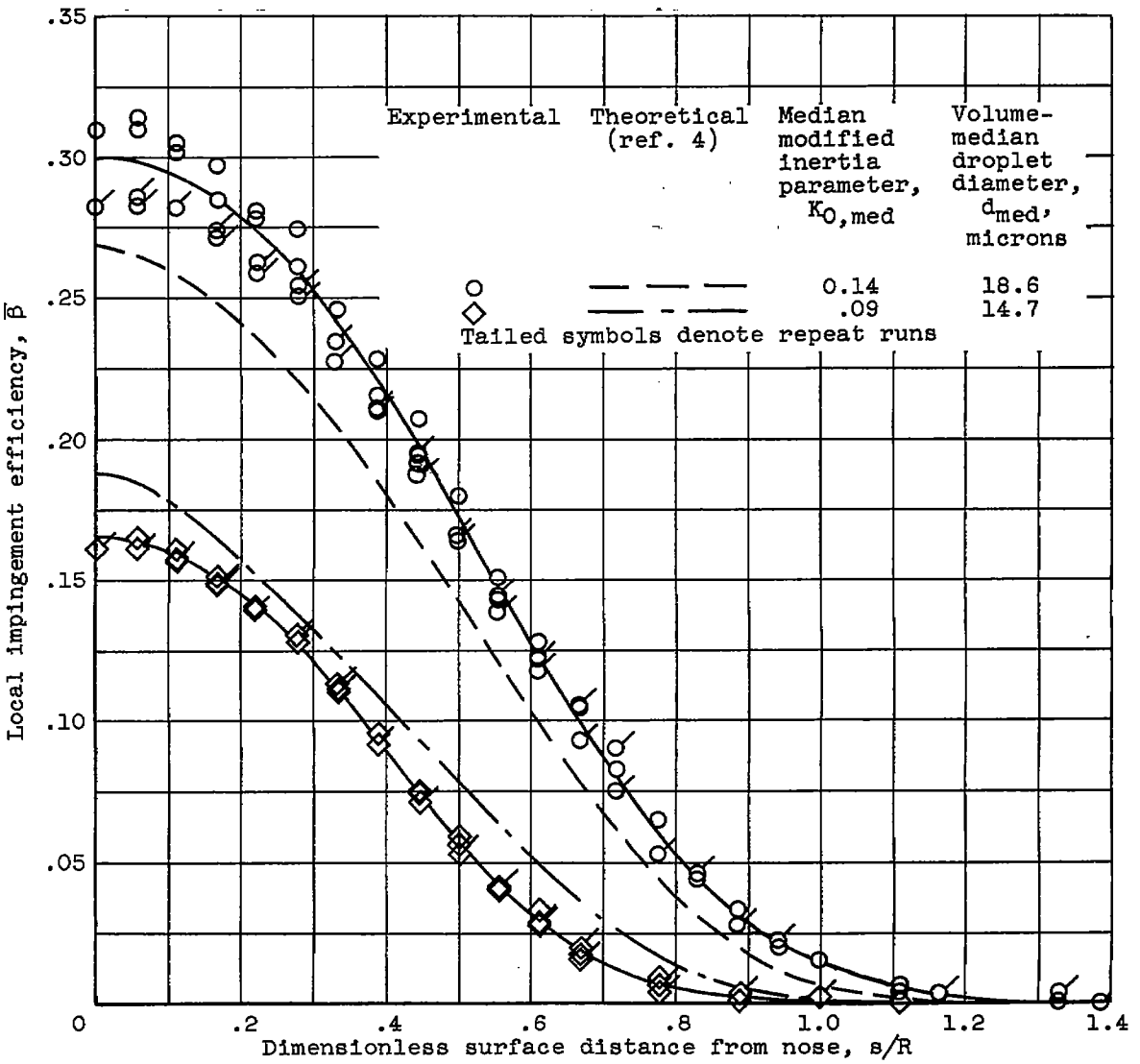

(b) Droplet diameters, 14.7 and 18.6 microns.

Figure 9. - Concluded. Comparison of experimental and theoretical local impingement efficiencies for 18-inch-diameter sphere at four droplet diameters.

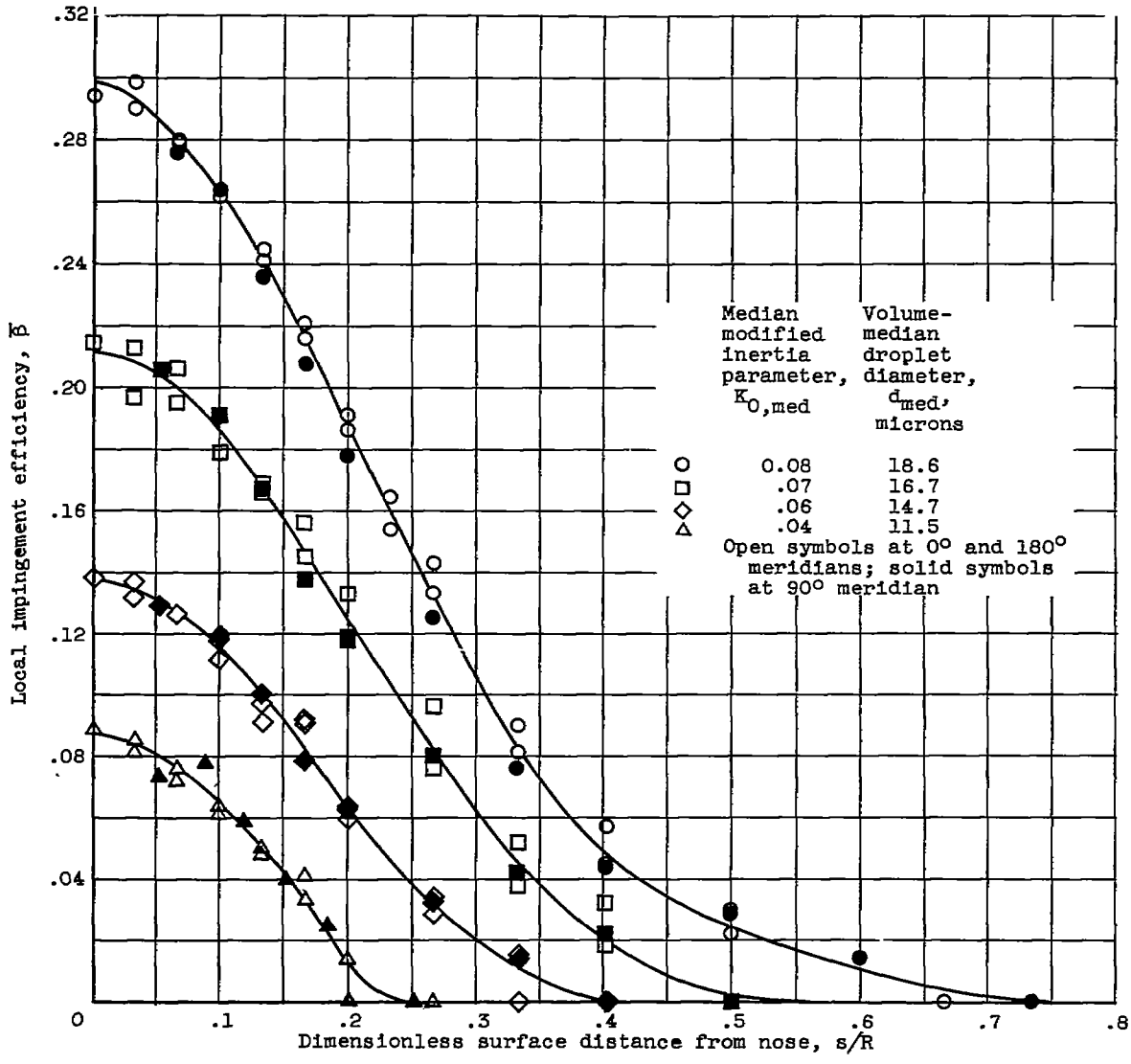

(a) Fineness ratio, 2.5; diameter, 30 inches.

Figure 10. - Variation of local impingement efficiency over surface of two stationary ellipsoidal forebodies at zero angle of attack.

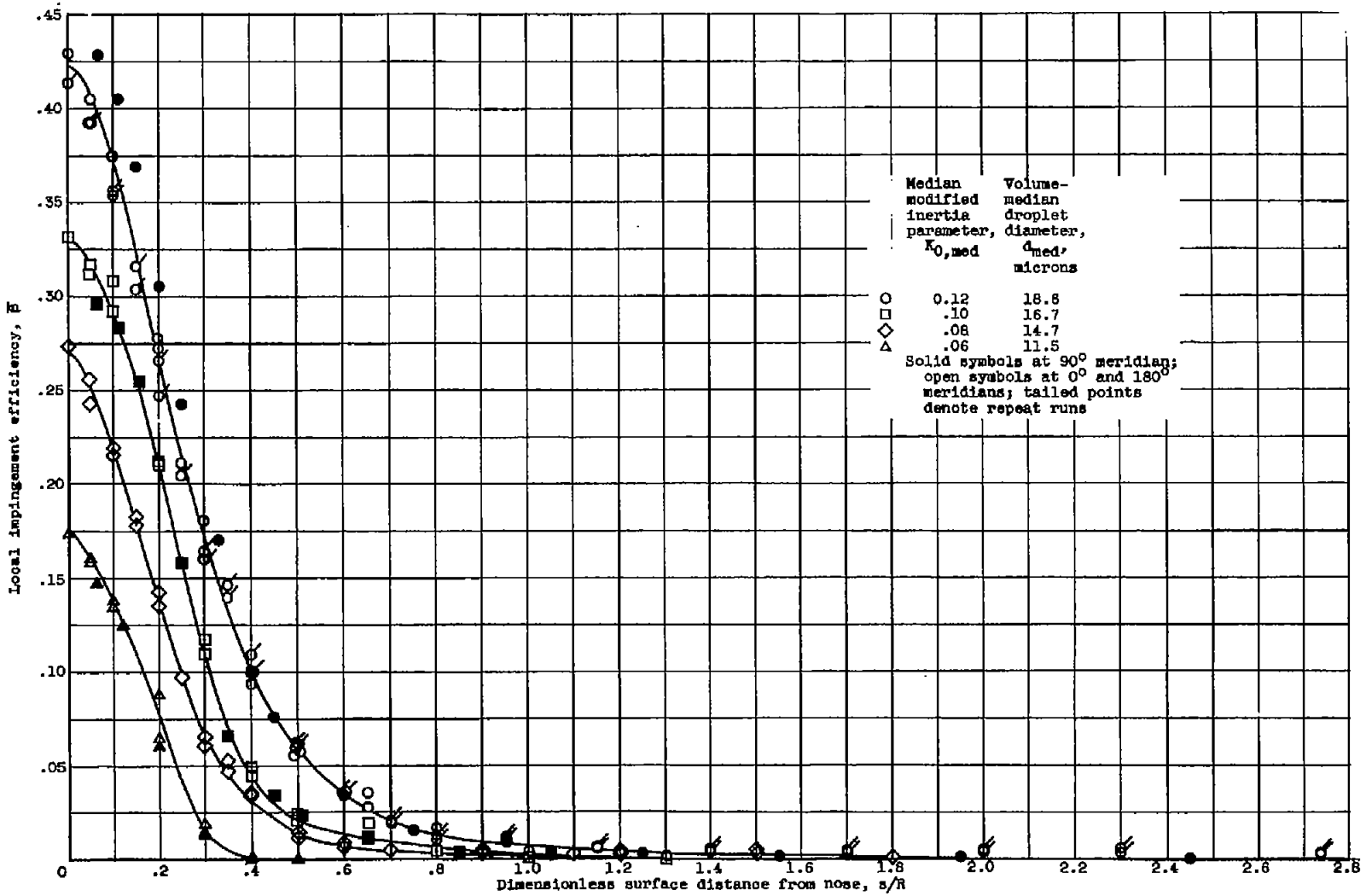

(b) Fineness ratio, 3.0; diameter, 20 inches.

Figure 10. - Concluded. Variation of local impingement efficiency over surface of two stationary ellipsoidal forebodies at zero angle of attack.

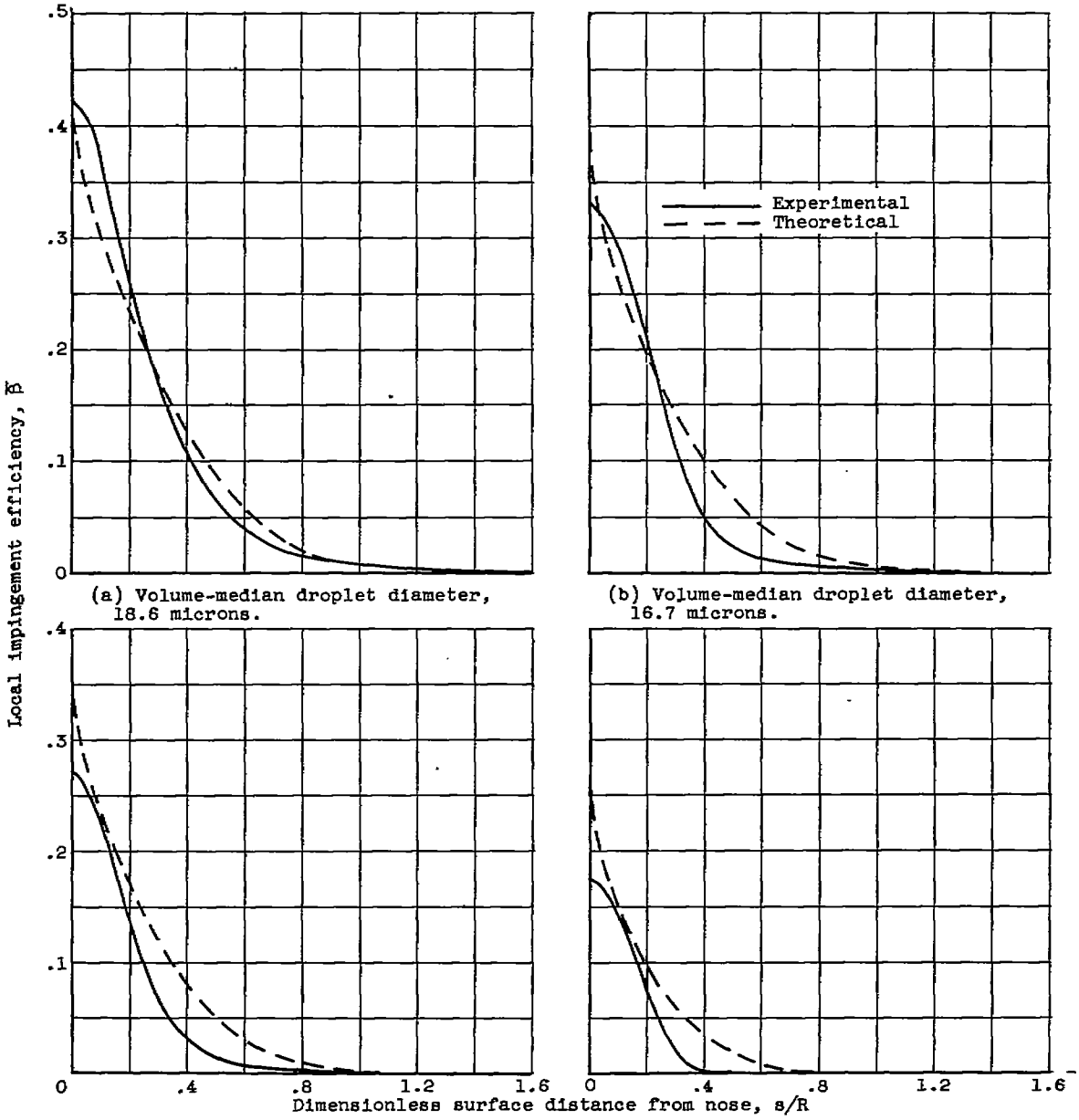

(a) Volume-median droplet diameter, 18.6 microns.

(b) Volume-median droplet diameter, 16.7 microns.

(c) Volume-median droplet diameter, 14.7 microns.

(d) Volume-median droplet diameter, 11.5 microns.

Figure 11. - Comparison of experimental and theoretical local impingement efficiencies for ellipsoid of fineness ratio of 3.0 at four droplet diameters and zero angle of attack.

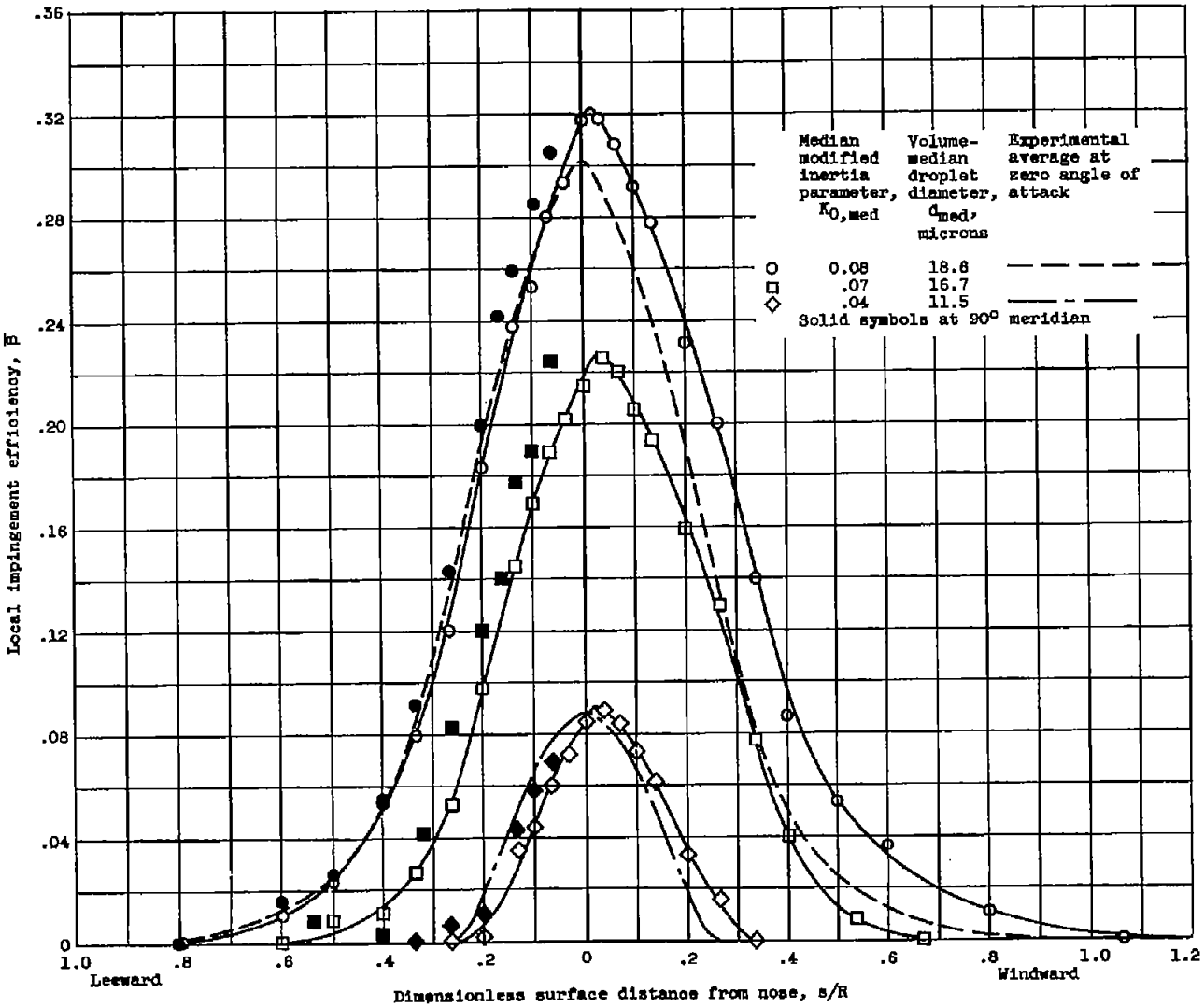

(a) Fineness ratio, 2.5; angle of attack, 5°.

Figure 12. - Effect of angle of attack on local impingement efficiency of two stationary ellipsoidal forebodies.

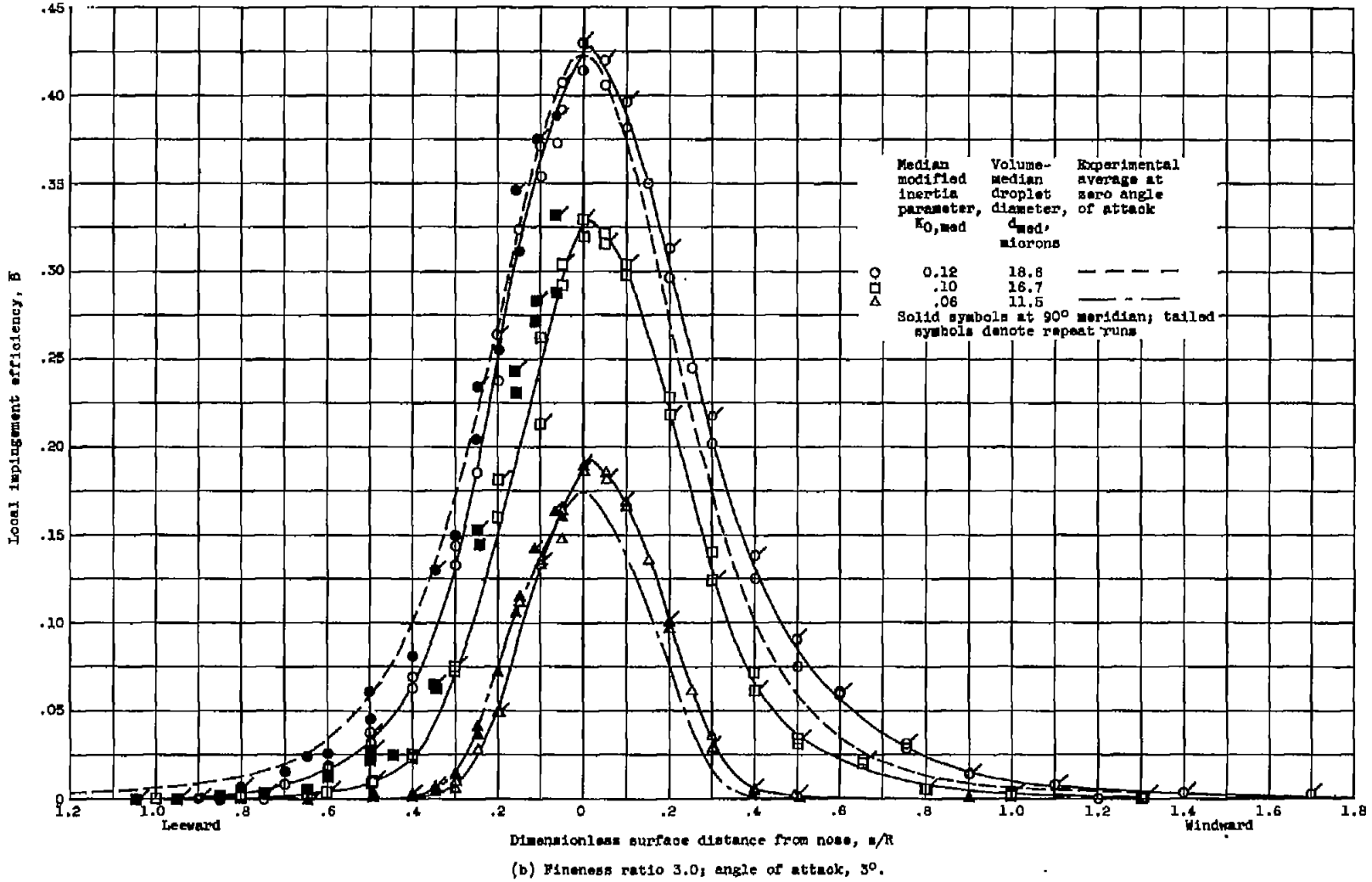

(b) Fineness ratio 3.0; angle of attack, 3°.

Figure 12. - Continued. Effect of angle of attack on local impingement efficiency of two stationary ellipsoidal forebodies.

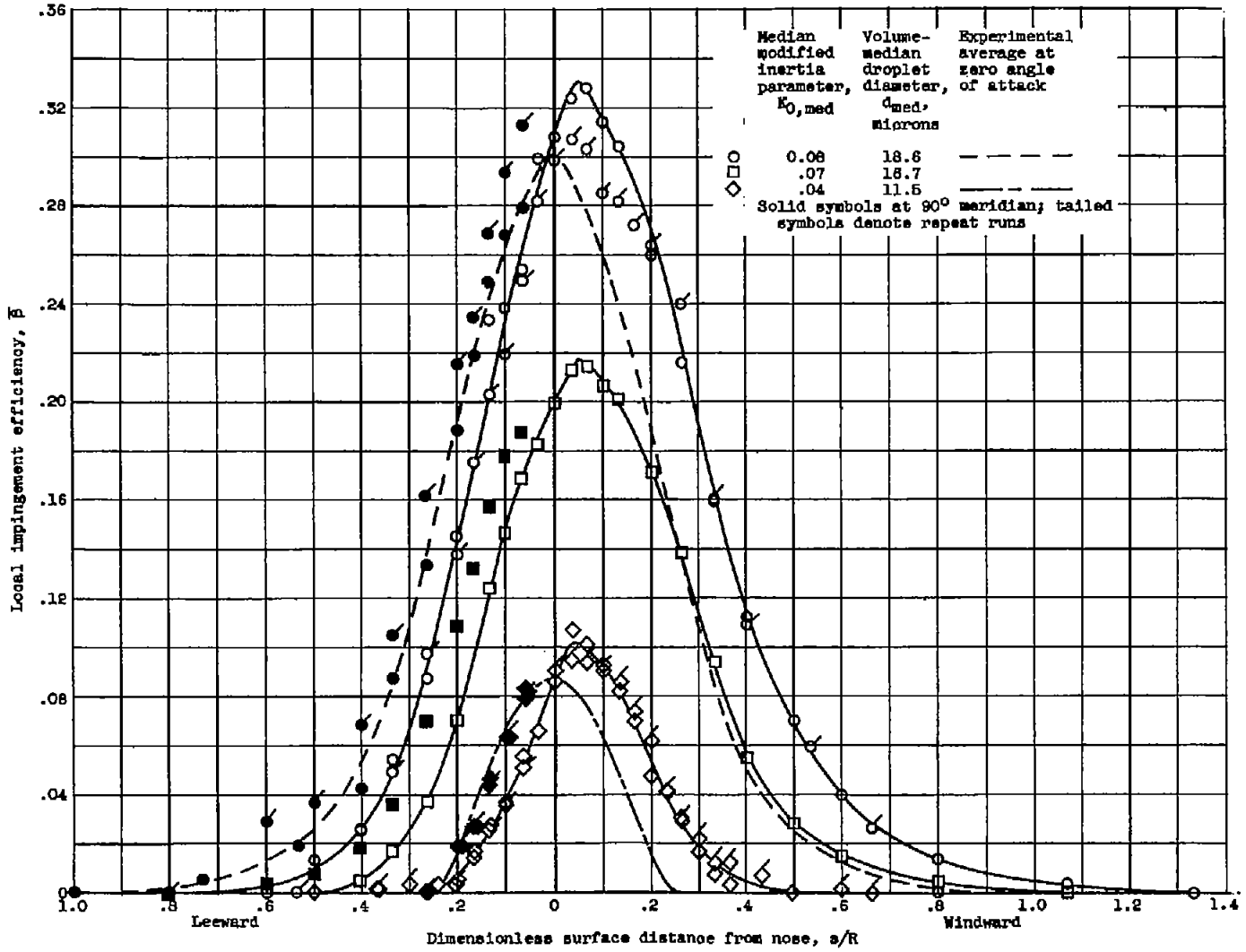

(c) Fineness ratio, 2.5; angle of attack, 6°.

Figure 12. - Continued. Effect of angle of attack on local impingement efficiency of two stationary ellipsoidal forebodies.

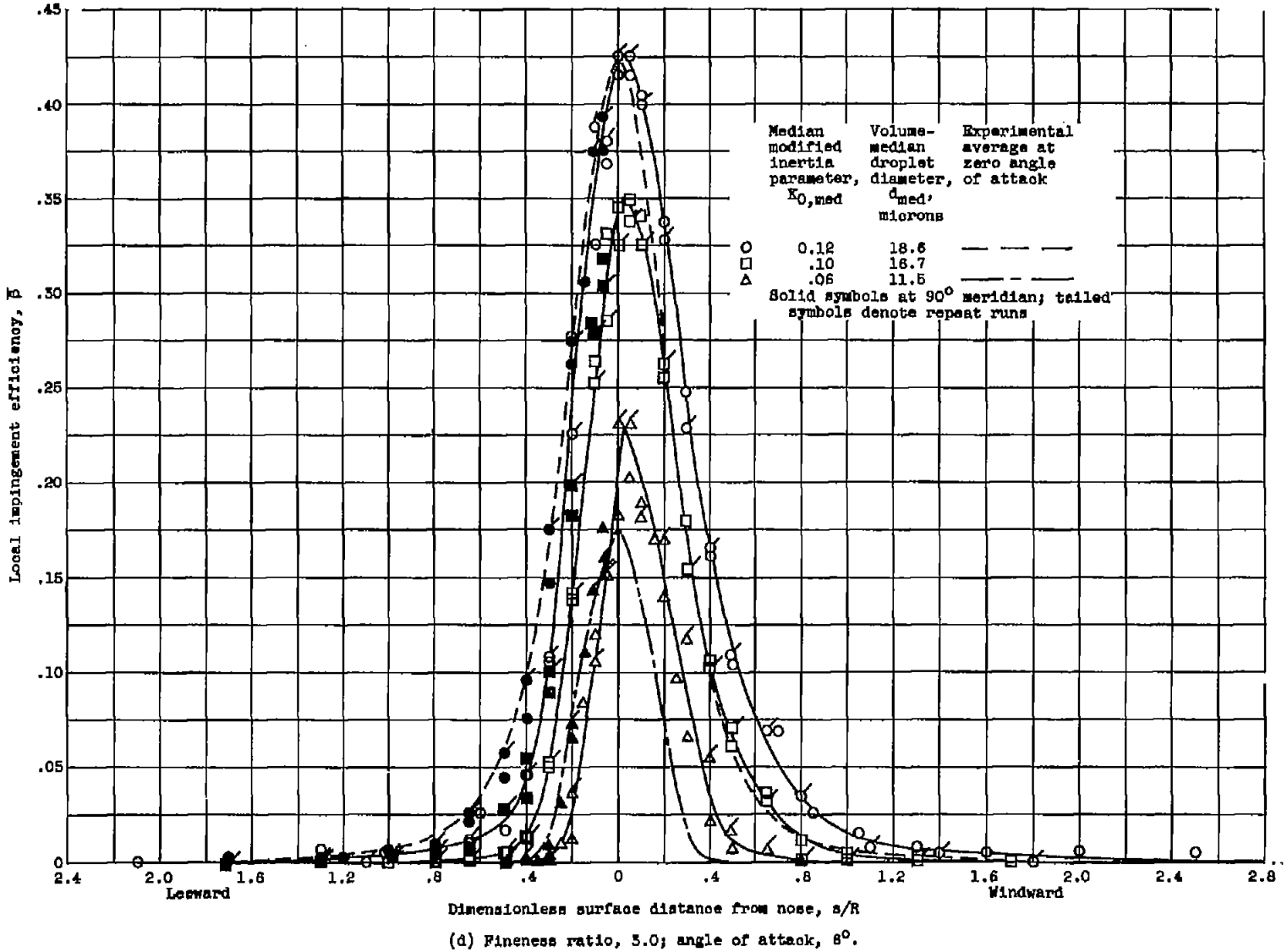

(d) Fineness ratio, 3.0; angle of attack, 8°.

Figure 12. - Concluded. Effect of angle of attack on local impingement efficiency of two stationary ellipsoidal forebodies.

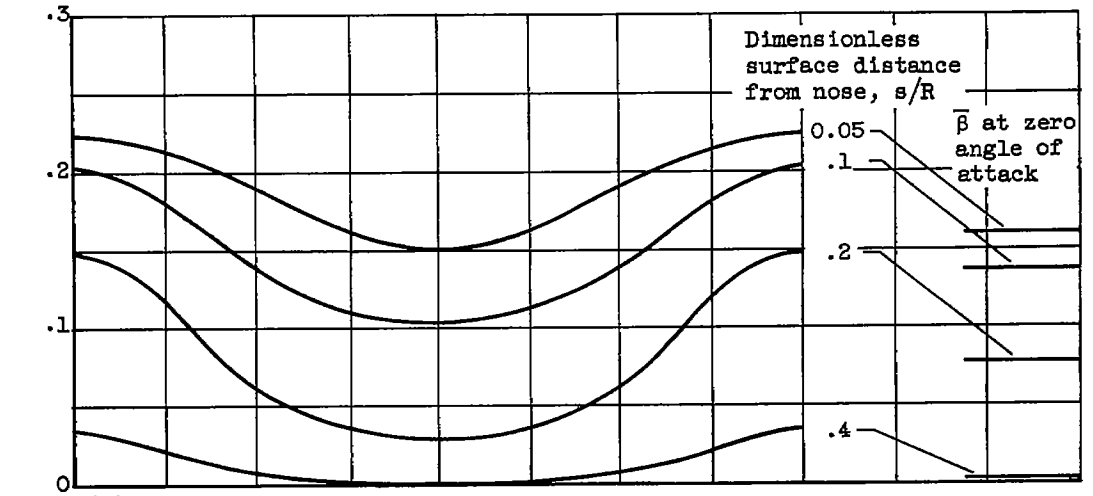

(a) Fineness ratio, 3.0; droplet diameter, 11.5 microns; median modified inertia parameter, 0.06.

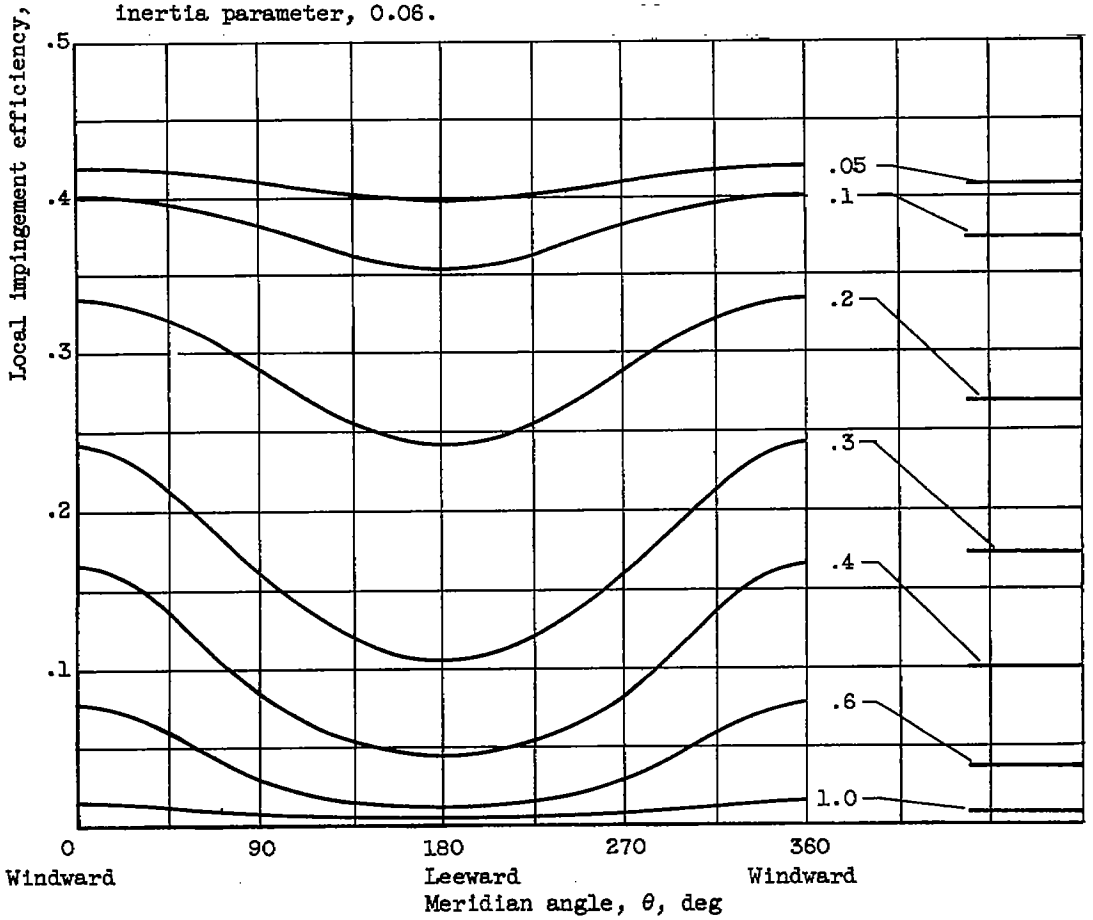

(b) Fineness ratio, 3.0; droplet diameter, 18.6 microns; median modified inertia parameter, 0.12.

Figure 13. - Peripheral variation of local impingement efficiency on ellipsoids at angle of attack of 6° at two droplet diameters.

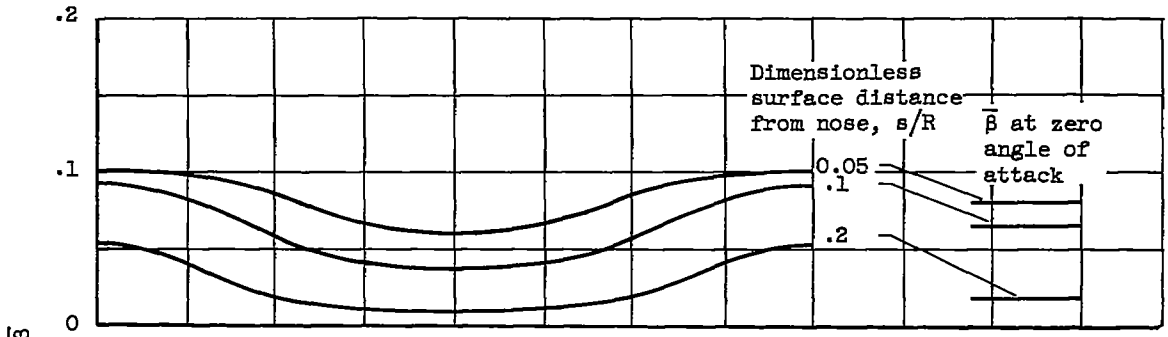

(c) Fineness ratio, 2.5; droplet diameter, 11.5 microns; median modified inertia parameter, 0.04.

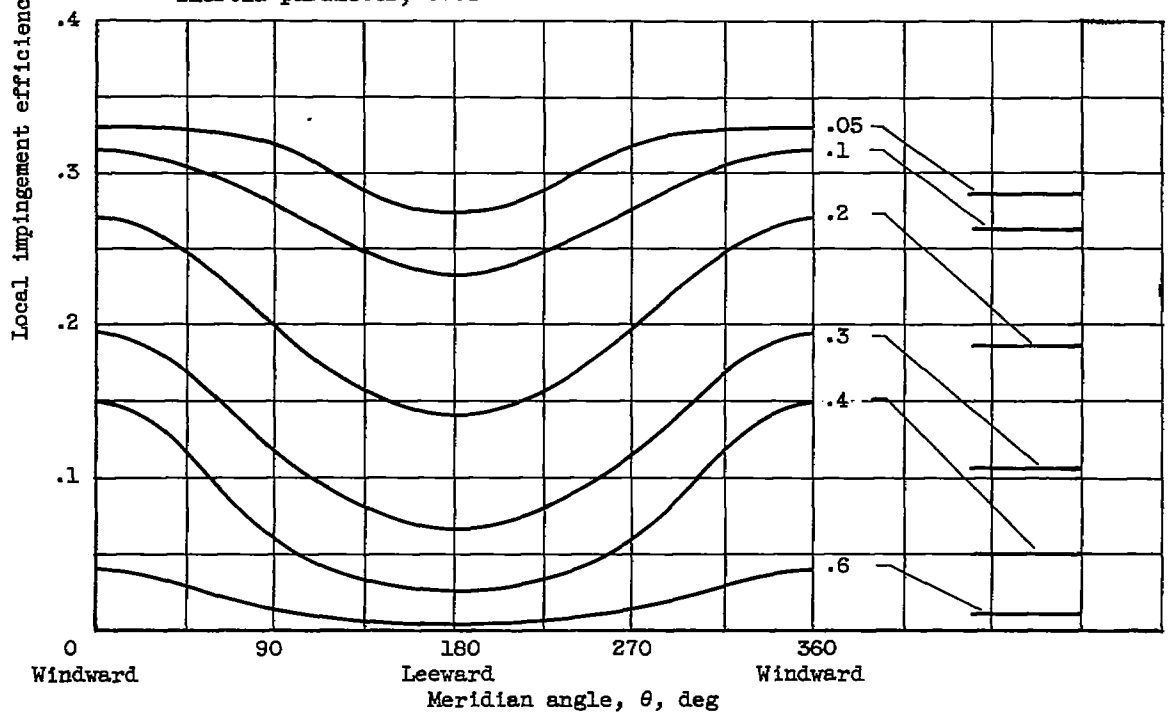

(d) Fineness ratio, 2.5; droplet diameter, 18.6 microns; median modified inertia parameter, 0.08.

Figure 13. - Concluded. Peripheral variation of local impingement efficiency on ellipsoids at angle of attack of 6° at two droplet diameters.

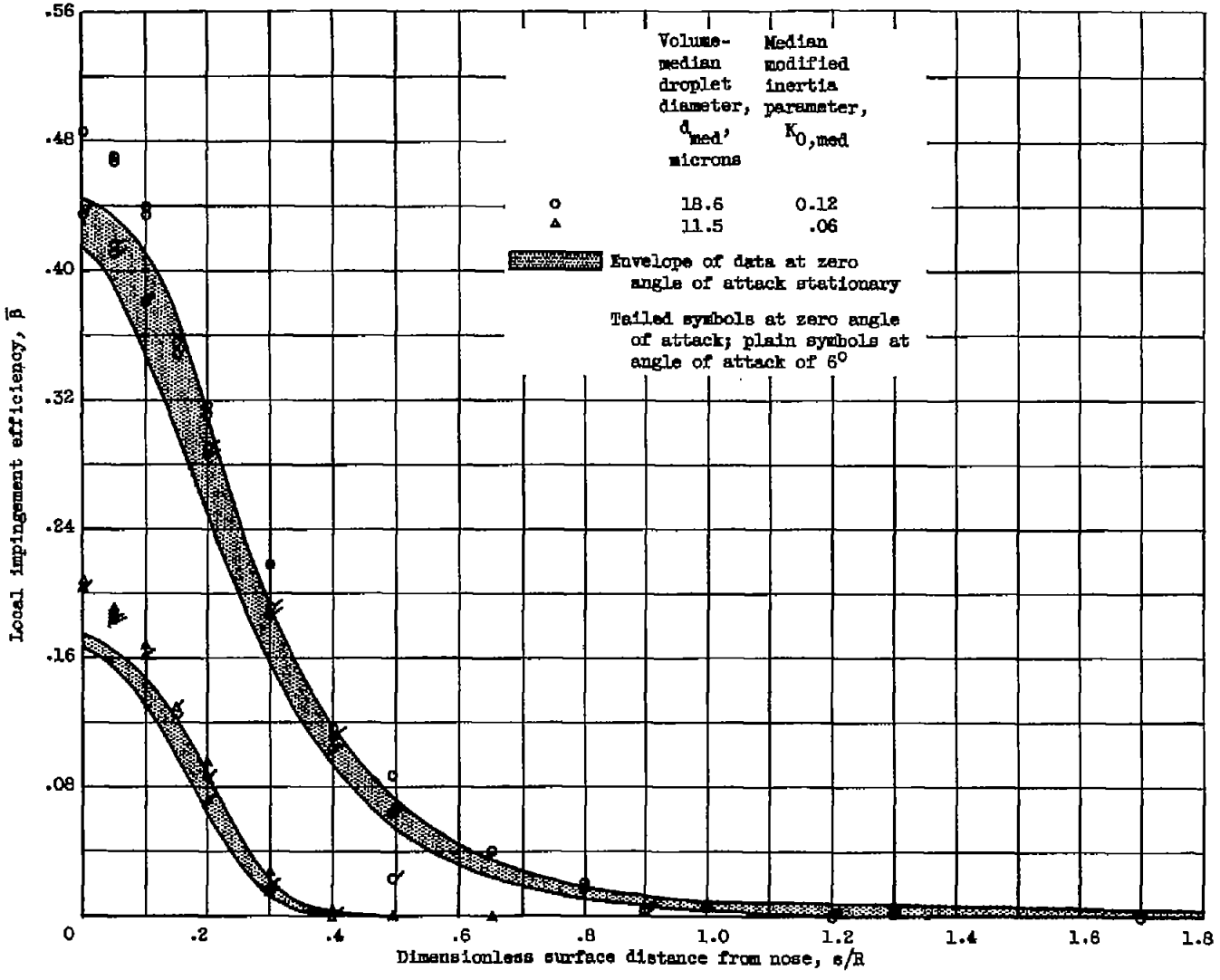

(a) Fineness ratio, 3.0; rotational speed, 800 rpm.

Figure 14. - Effect of rotation on local impingement efficiency of ellipsoids.

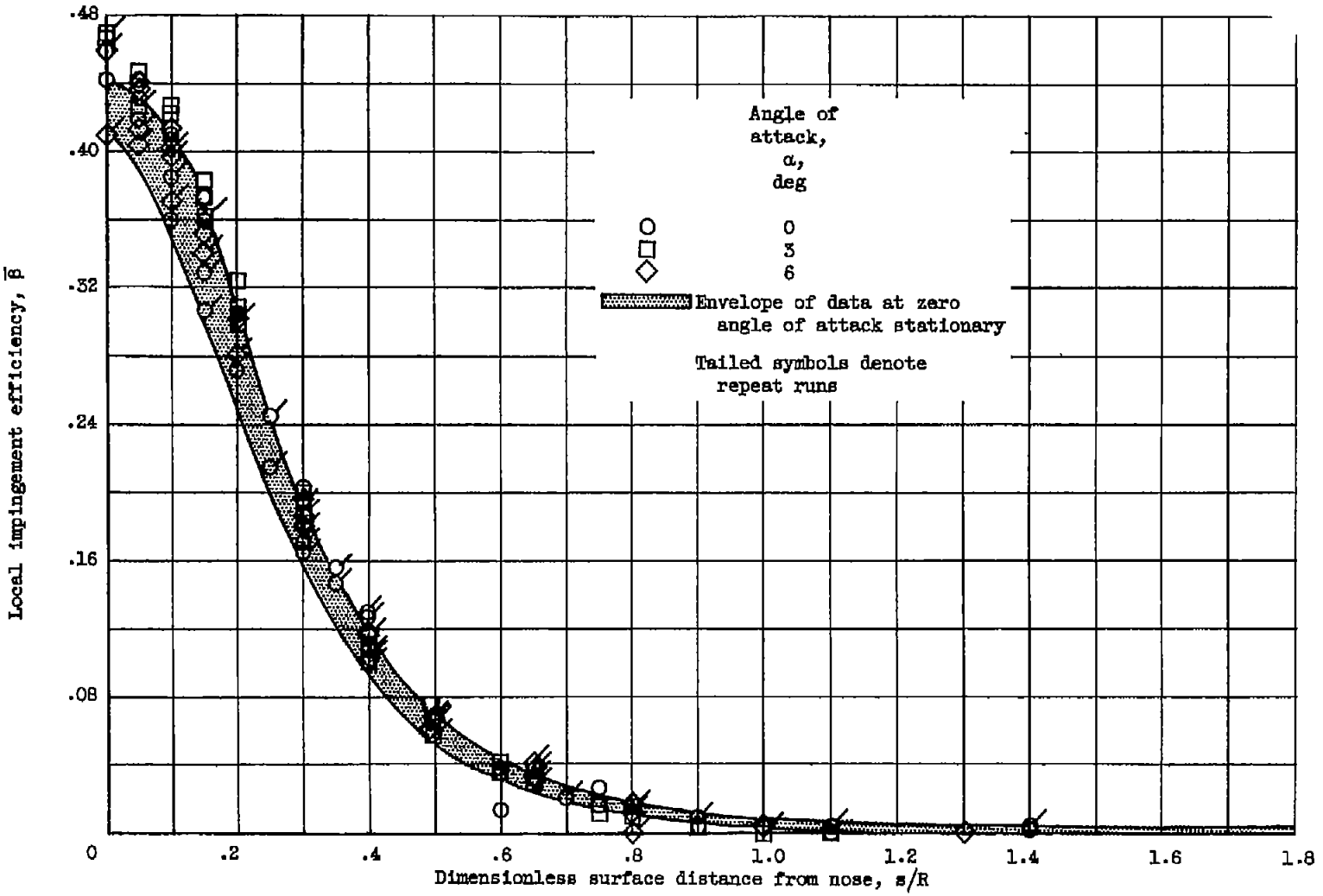

(b) Fineness ratio, 3.0; volume-median droplet diameter, 18.6 microns; median modified inertia parameter, 0.12; rotational speed, 1200 rpm.

Figure 14. - Continued. Effect of rotation on local impingement efficiency of ellipsoids.

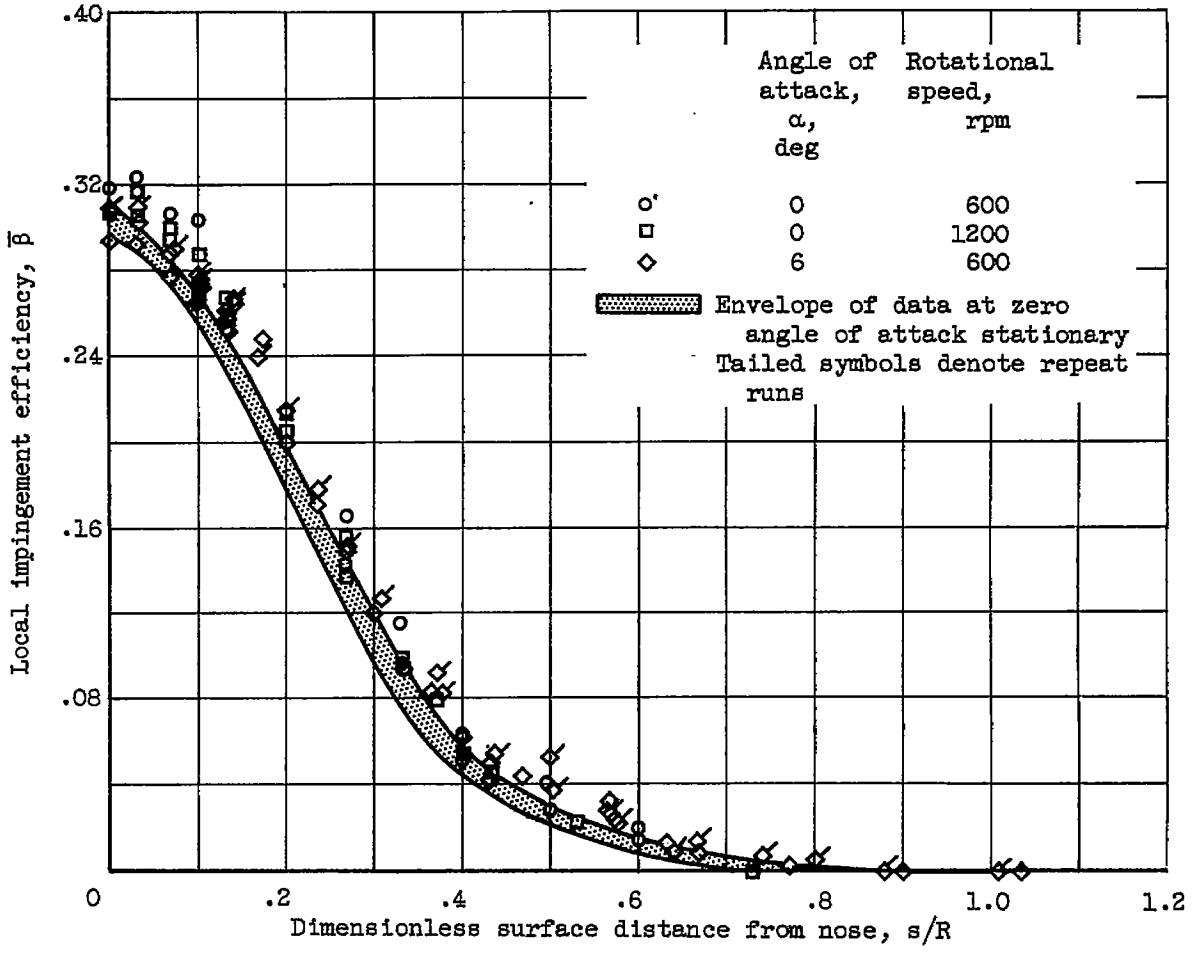

(c) Fineness ratio, 2.5; volume-median droplet diameter, 18.6 microns; median modified inertia parameter, 0.08.

Figure 14. - Concluded. Effect of rotation on local impingement efficiency of ellipsoids.

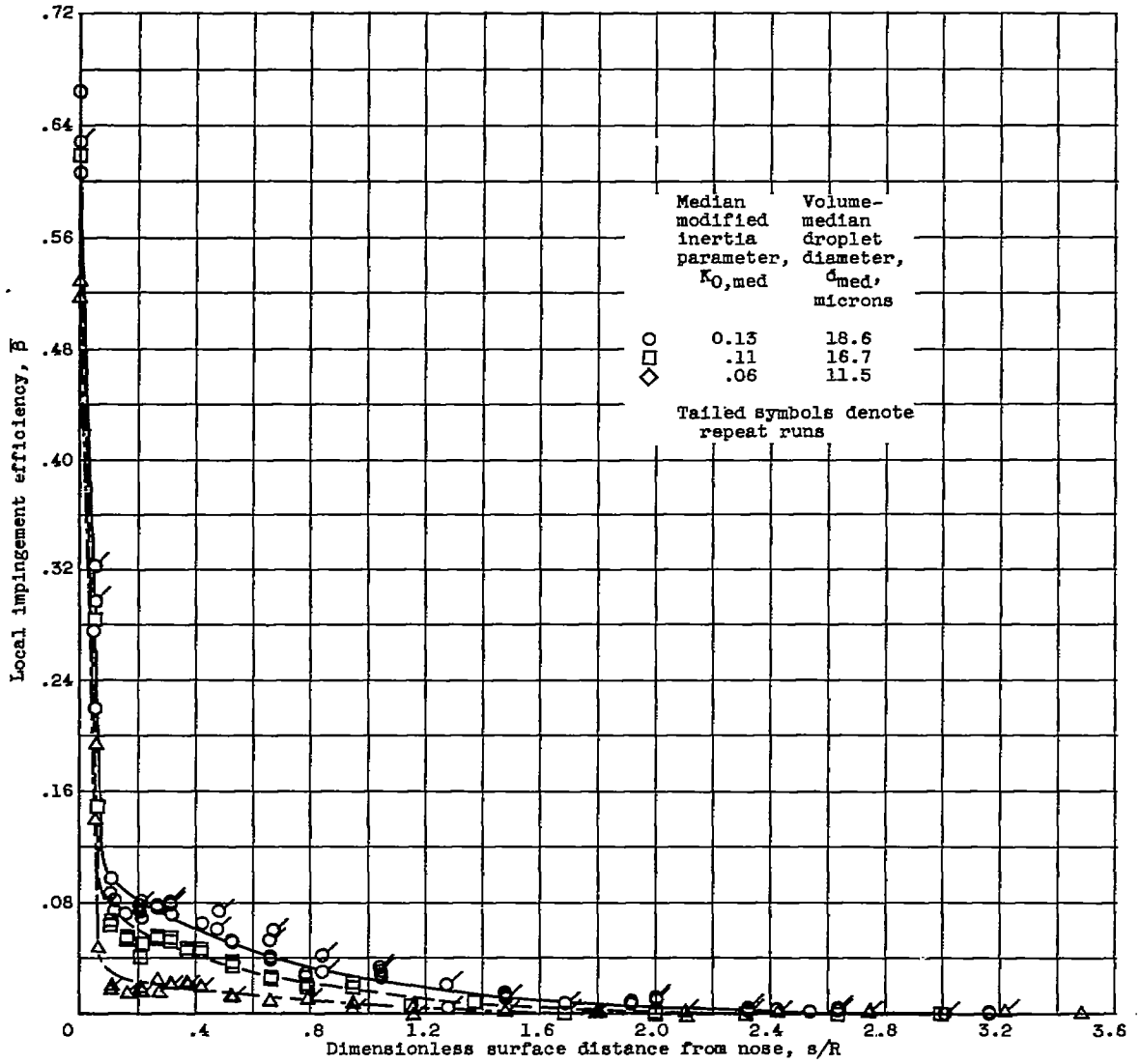

Figure 15. - Local impingement efficiency on stationary conical forebody at zero angle of attack.

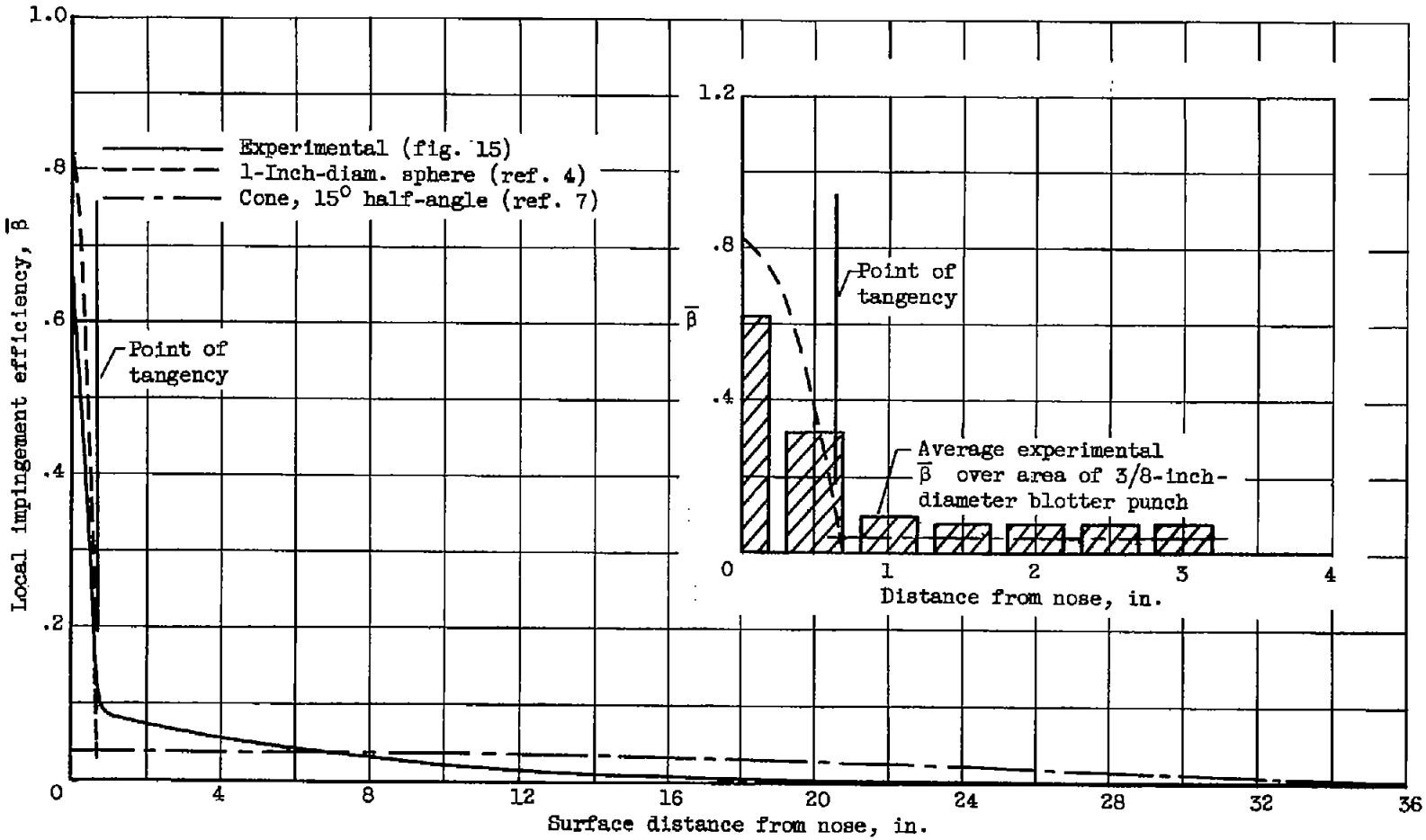

(a) Median modified inertia parameter, 0.13.

Figure 16. - Comparison of experimental and theoretical local impingement efficiency on stationary conical forebody at zero angle of attack.

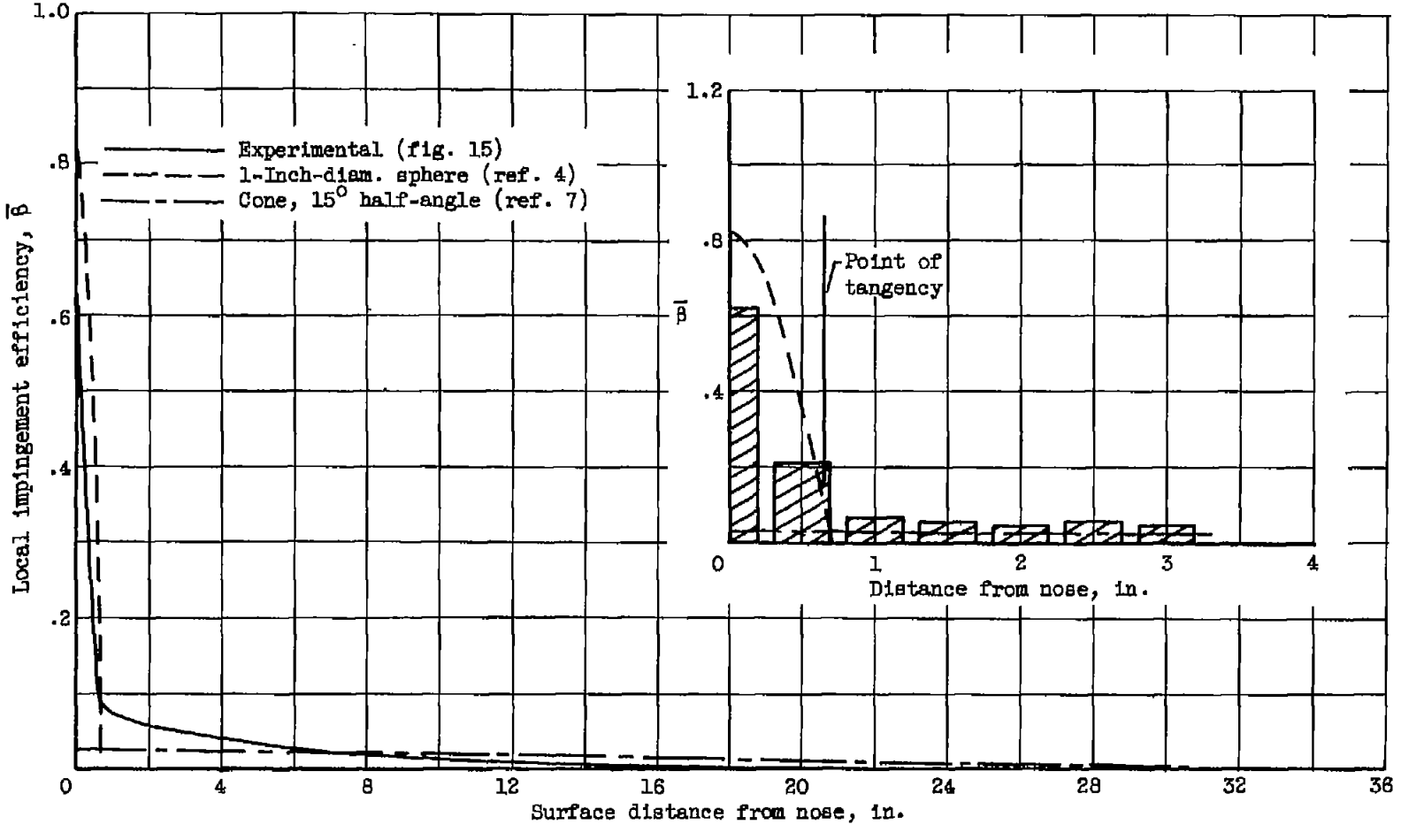

(b) Median modified inertia parameter, 0.11.

Figure 16. - Continued. Comparison of experimental and theoretical local impingement efficiency on stationary conical forebody at zero angle of attack.

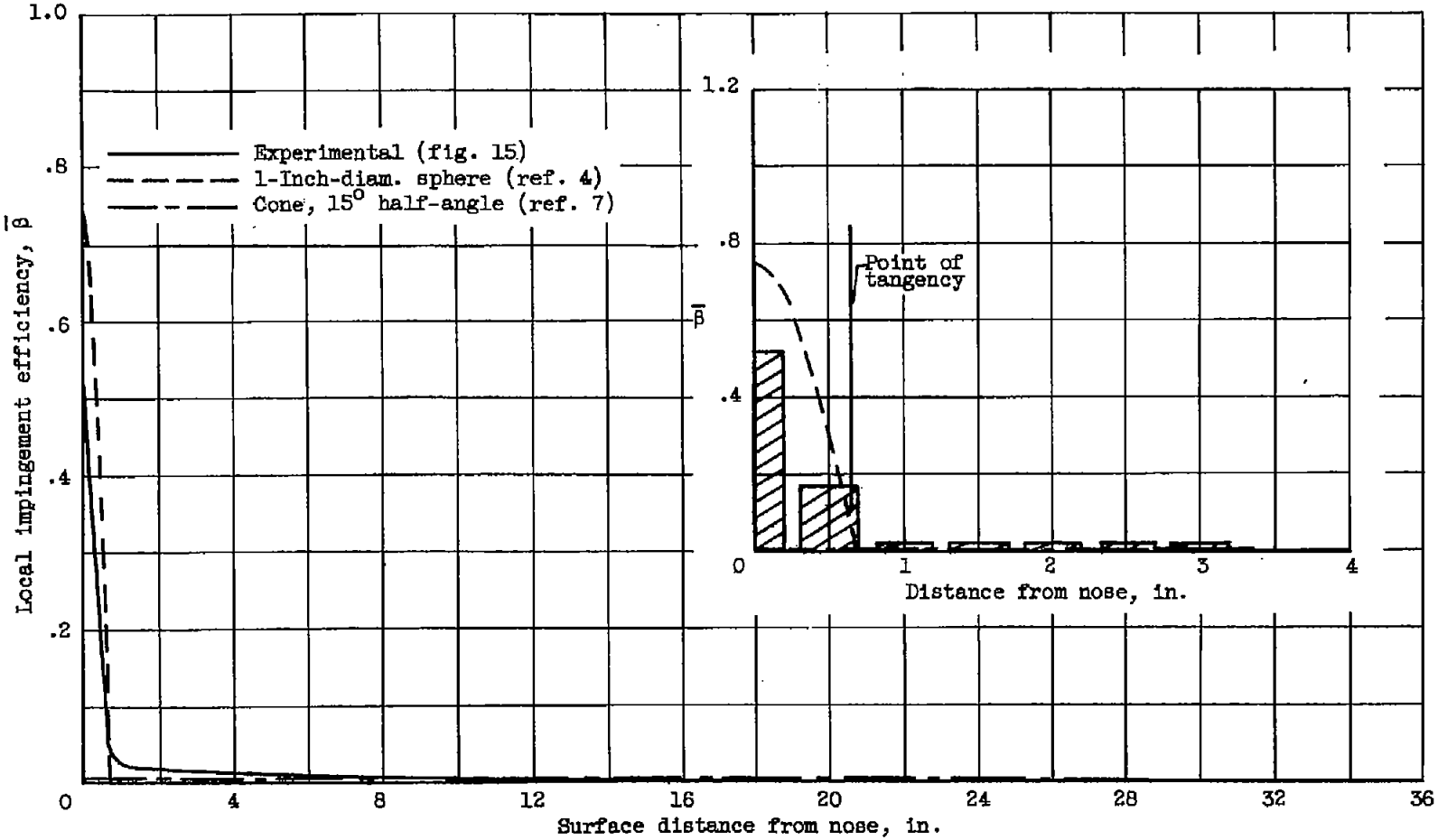

(c) Median modified inertia parameter, 0.06.

Figure 16. - Concluded. Comparison of experimental and theoretical local impingement efficiency on stationary conical forebody at zero angle of attack.

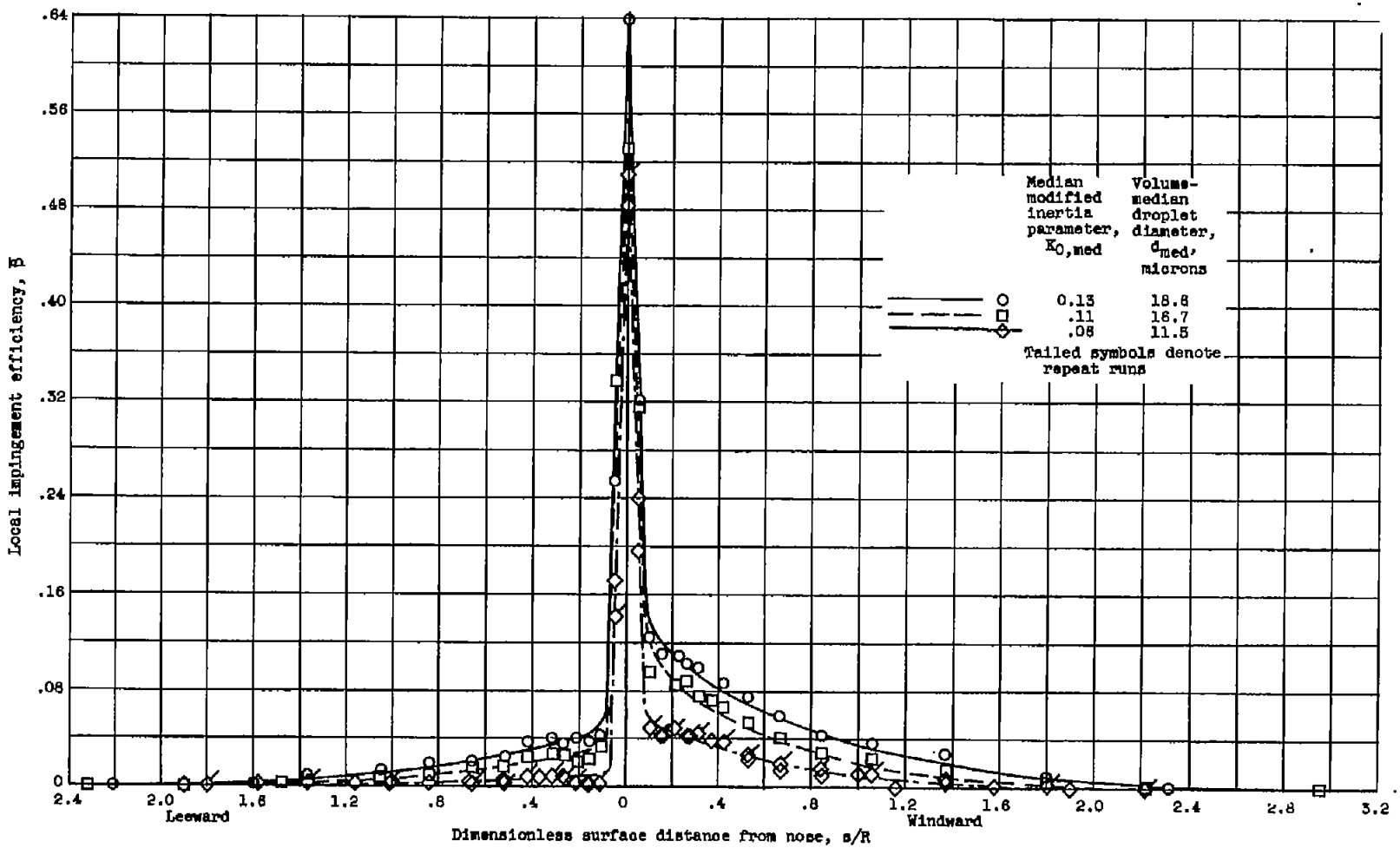

(a) Angle of attack, 3°.

Figure 17. - Local impingement efficiency on stationary conical forebody at angle of attack.

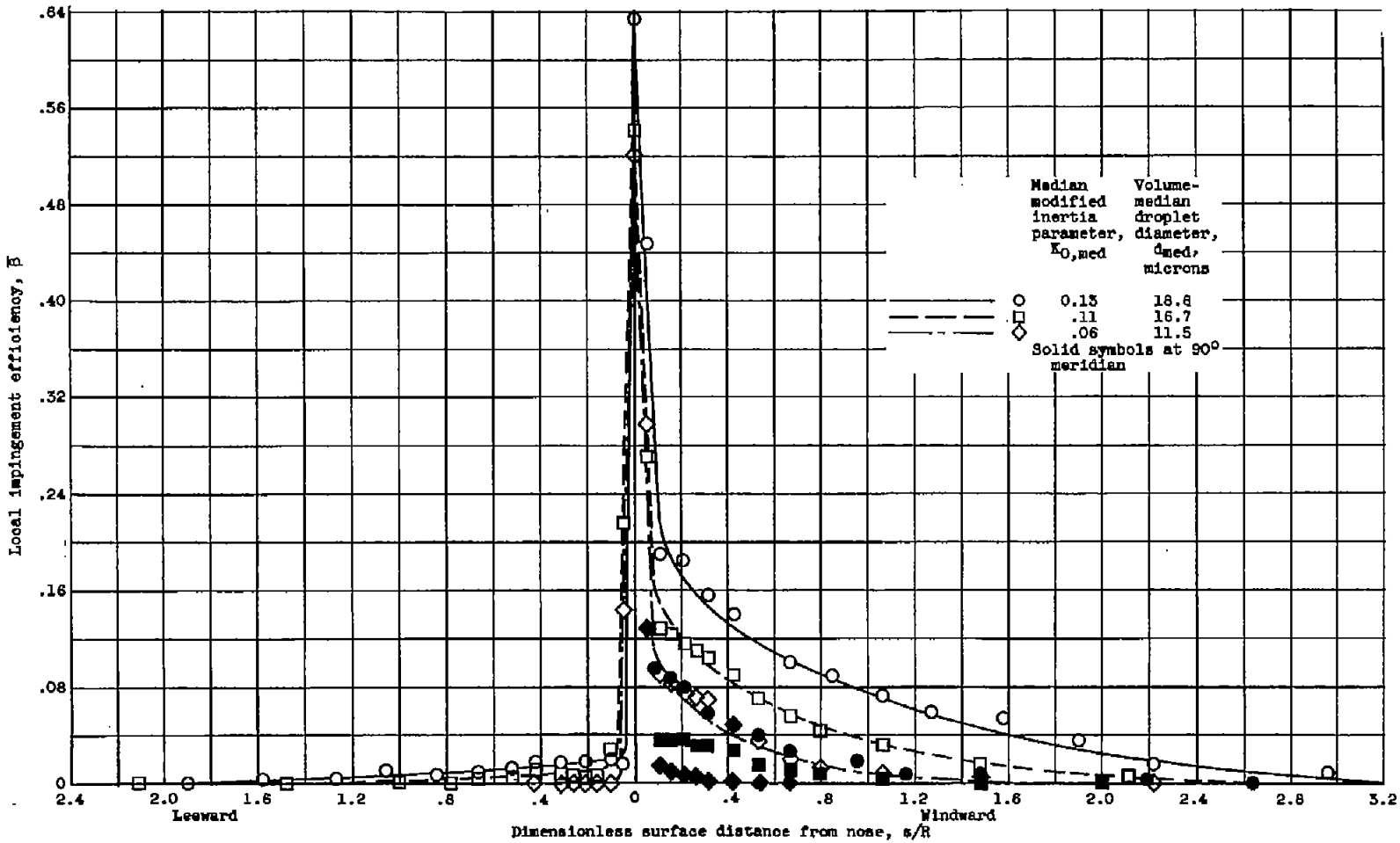

(b) Angle of attack, 6°.

Figure 17. - Continued. Local impingement efficiency on stationary conical forebody at angle of attack.

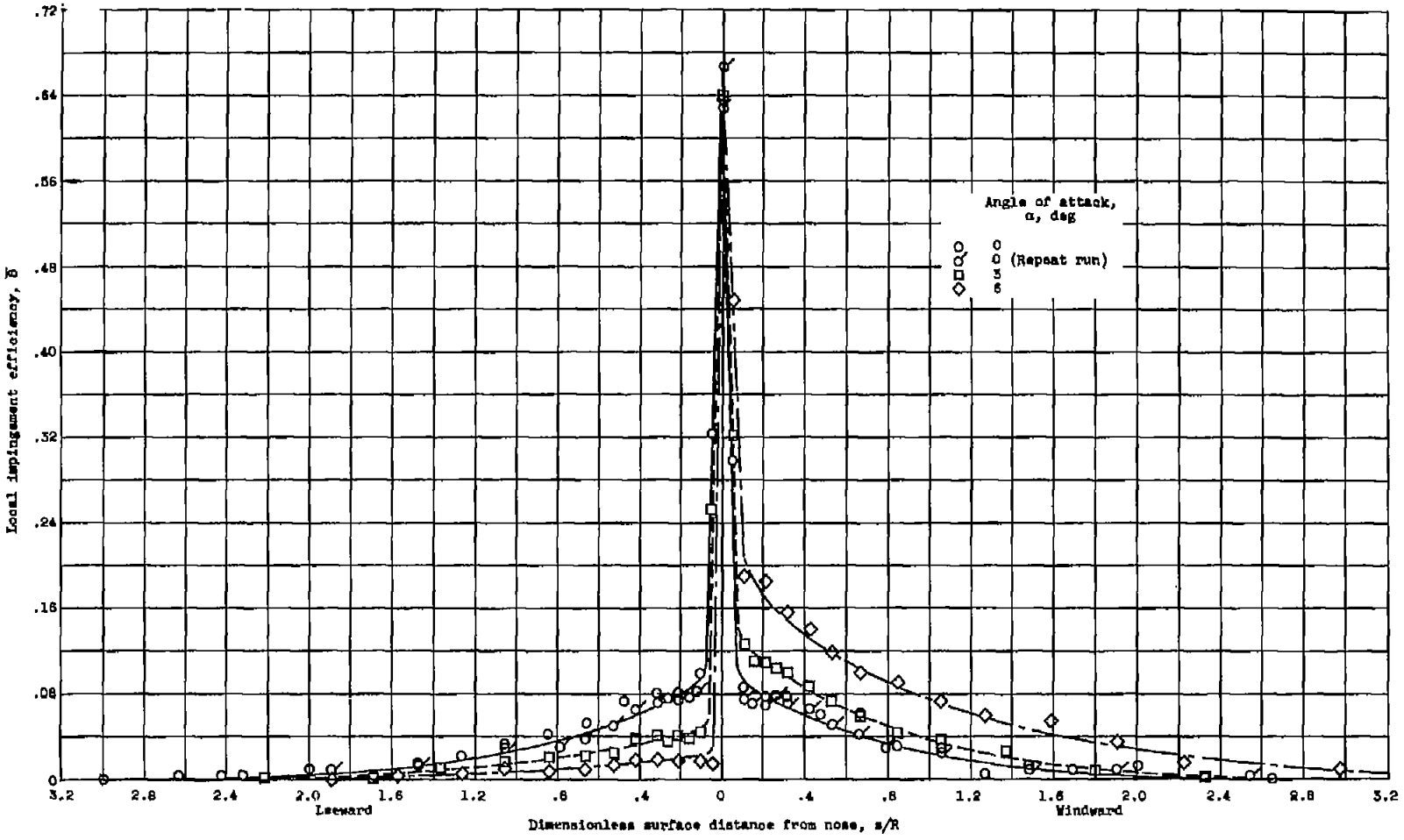

(c) Volume-median droplet diameter, 18.6 microns.

Figure 17. - Concluded. Local impingement efficiency on stationary conical forebody at angle of attack.

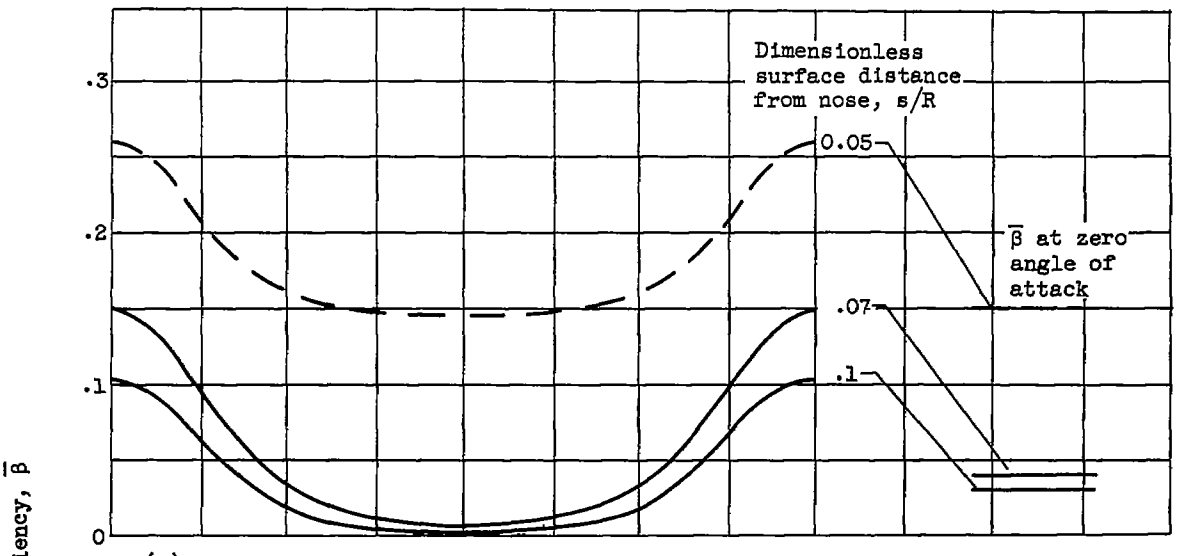

(a) Droplet diameter, 11.5 microns; median modified inertia parameter, 0.06.

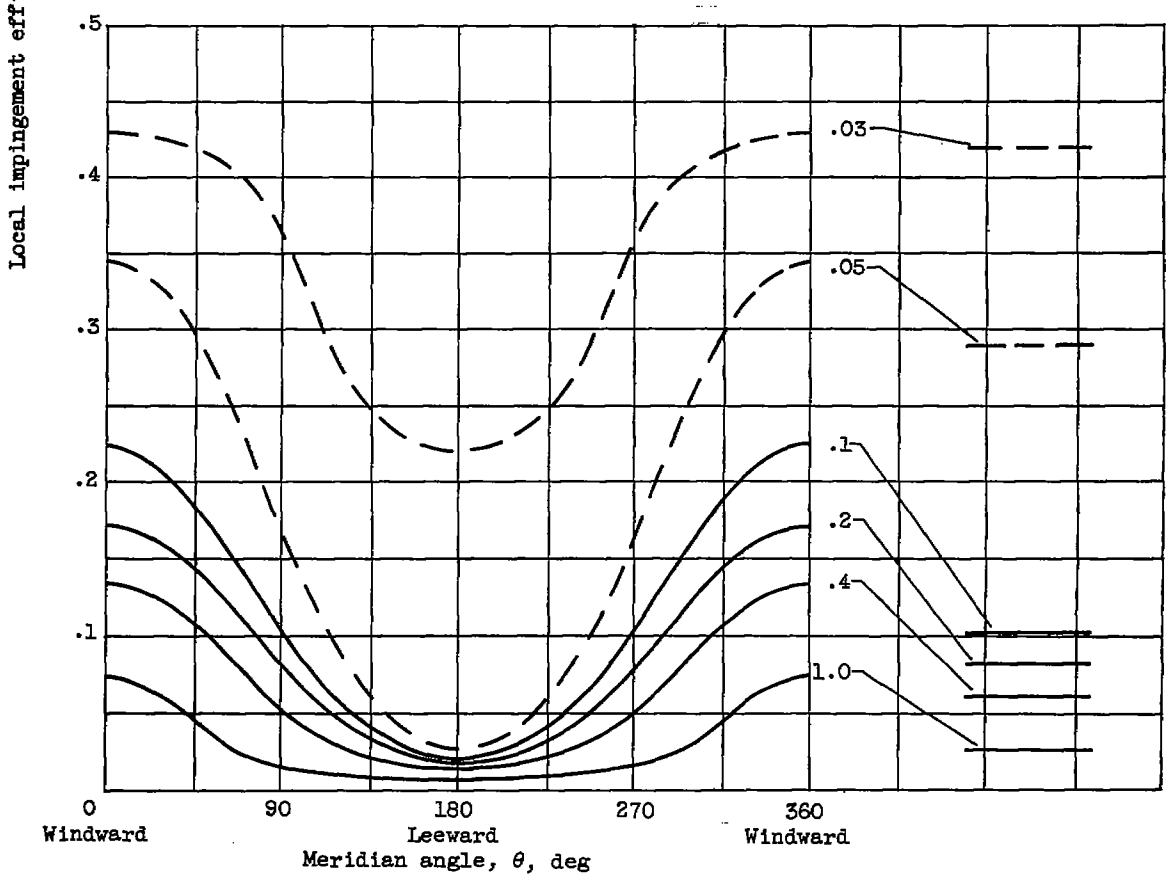

(b) Droplet diameter, 18.6 microns; median modified inertia parameter, 0.13.

Figure 18. - Peripheral variation of local impingement efficiency on conical forebody at angle of attack of 6° for two droplet diameters.

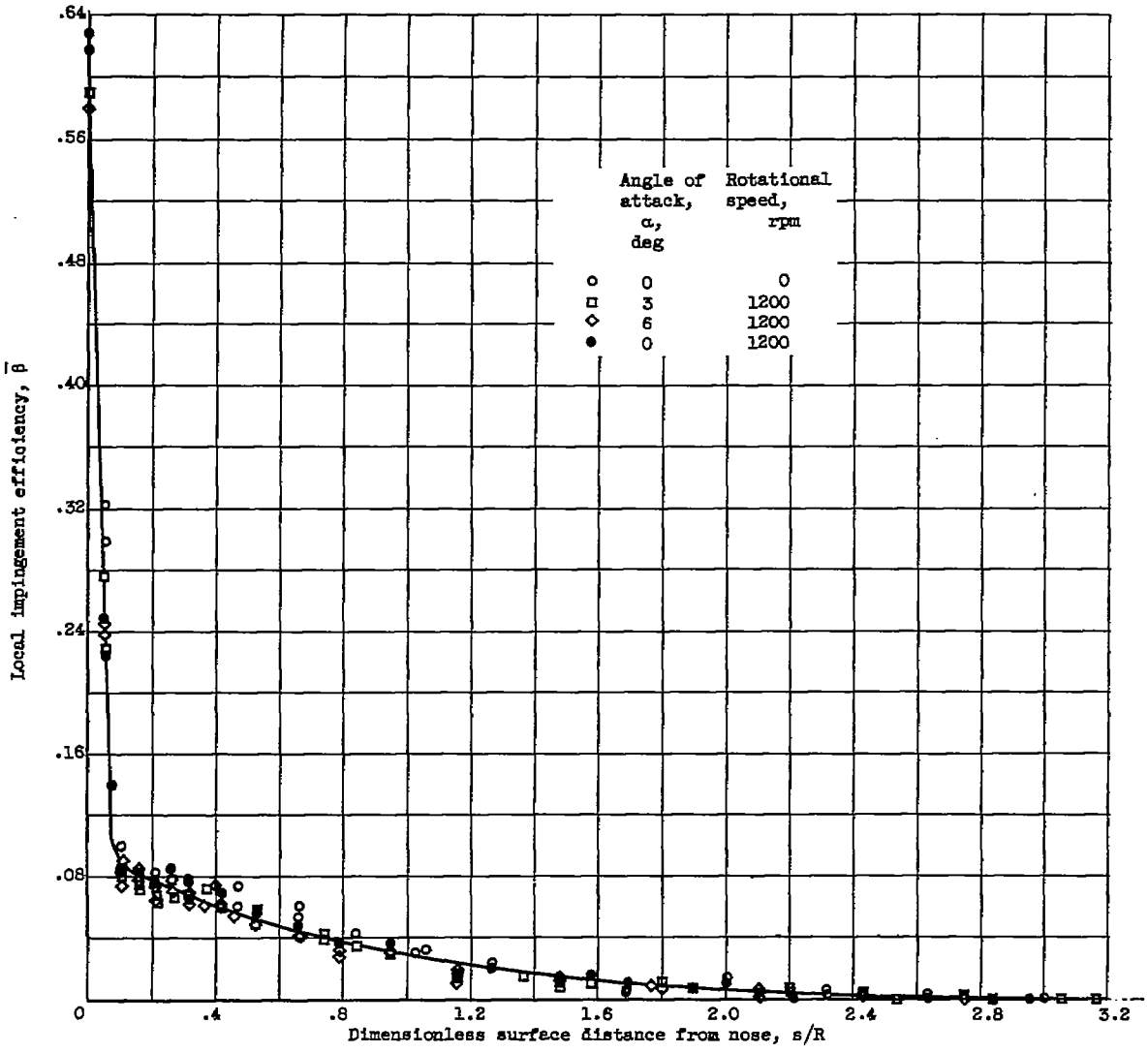

(a) Volume-median droplet diameter, 18.6 microns; median modified inertia parameter, 0.13.

Figure 19. - Effect of rotation on local impingement efficiency for conical forebody at several median droplet sizes and angles of attack.

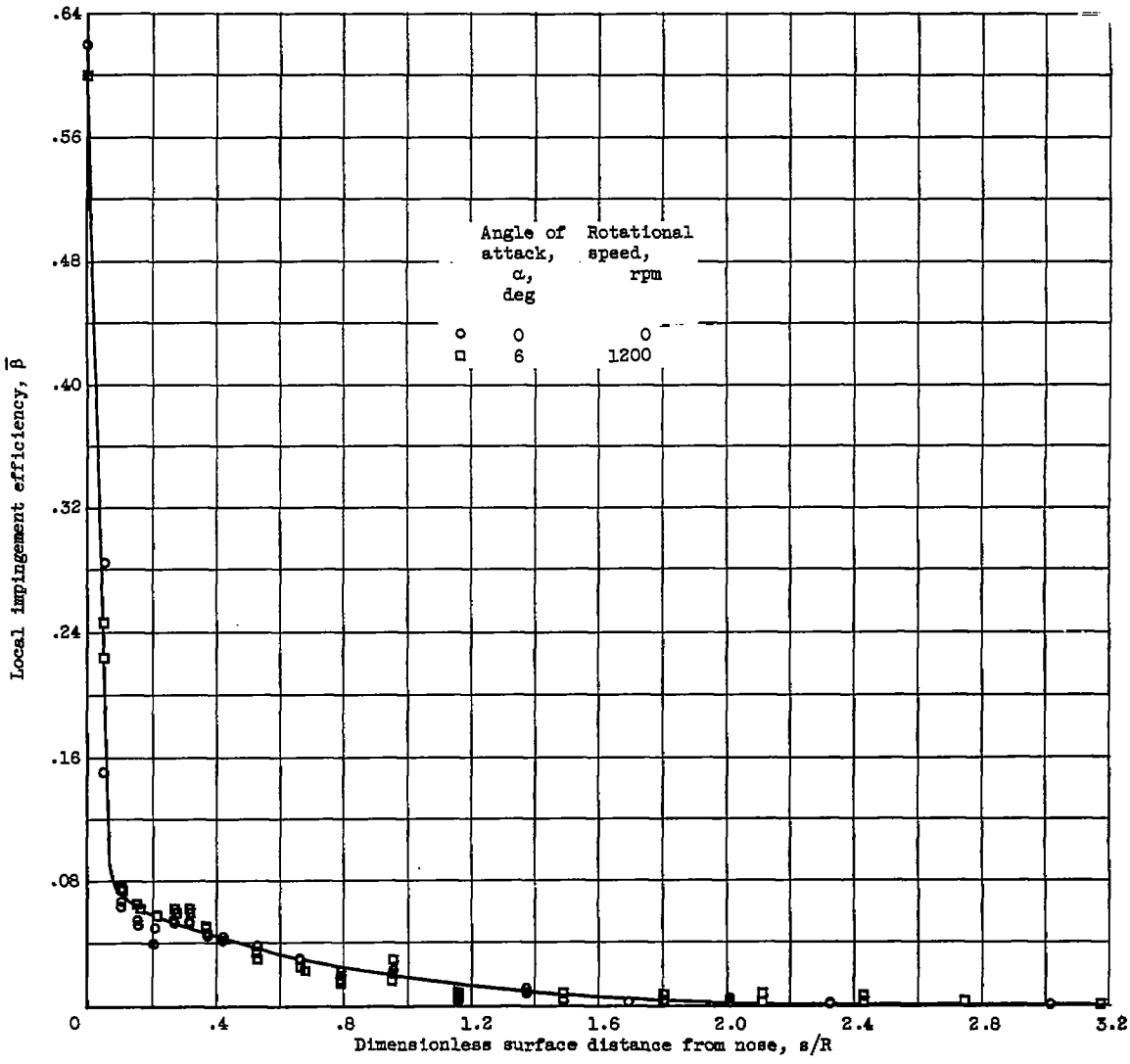

(b) Volume-median droplet diameter, 16.7 microns; median modified inertia parameter, 0.11.

Figure 19. - Continued. Effect of rotation on local impingement efficiency for conical forebody at several median droplet sizes and angles of attack.

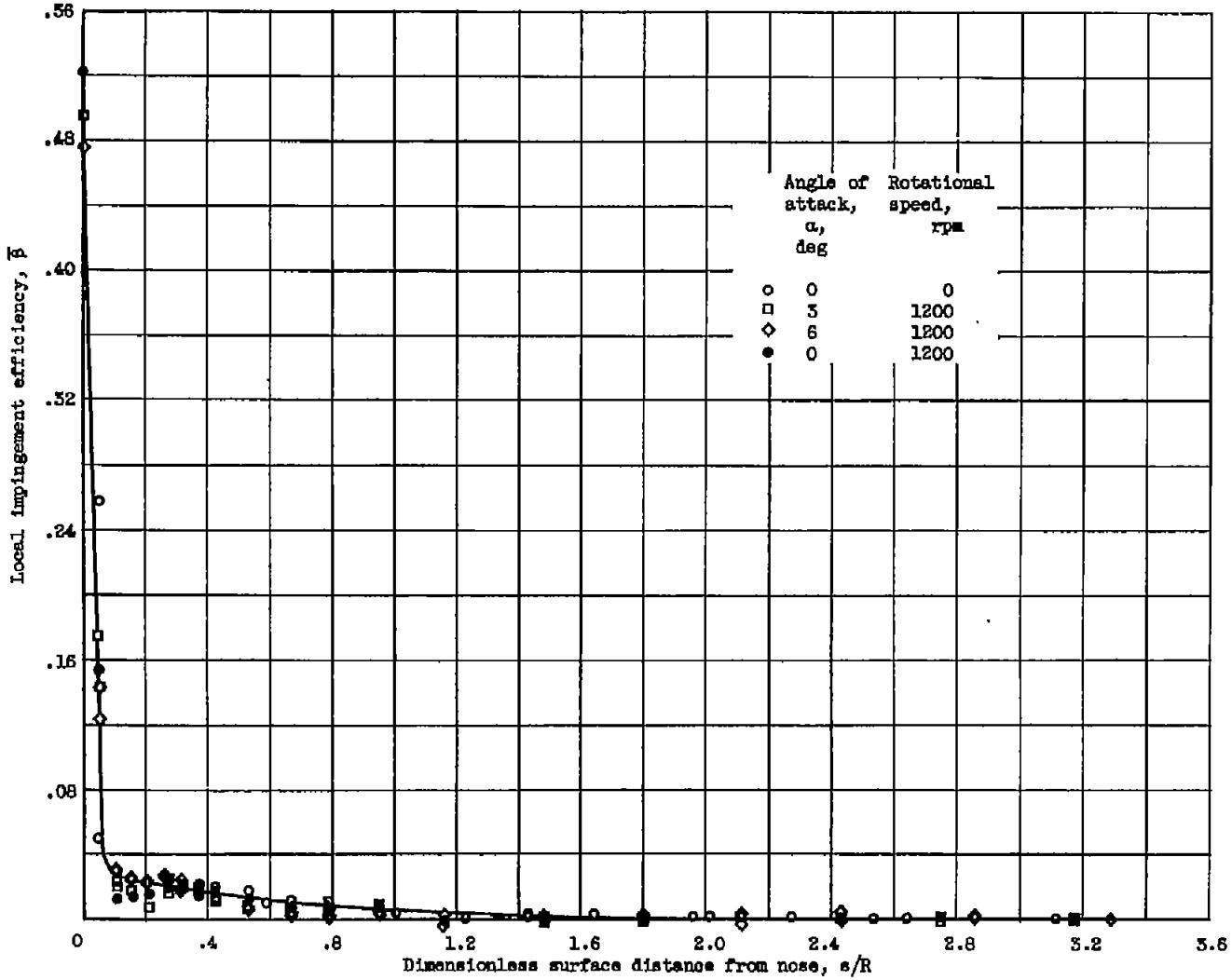

(c) Volume-median droplet diameter, 11.5 microns; median modified inertia parameter, 0.06.

Figure 19. - Concluded. Effect of rotation on local impingement efficiency for conical forebody at several median droplet sizes and angles of attack.

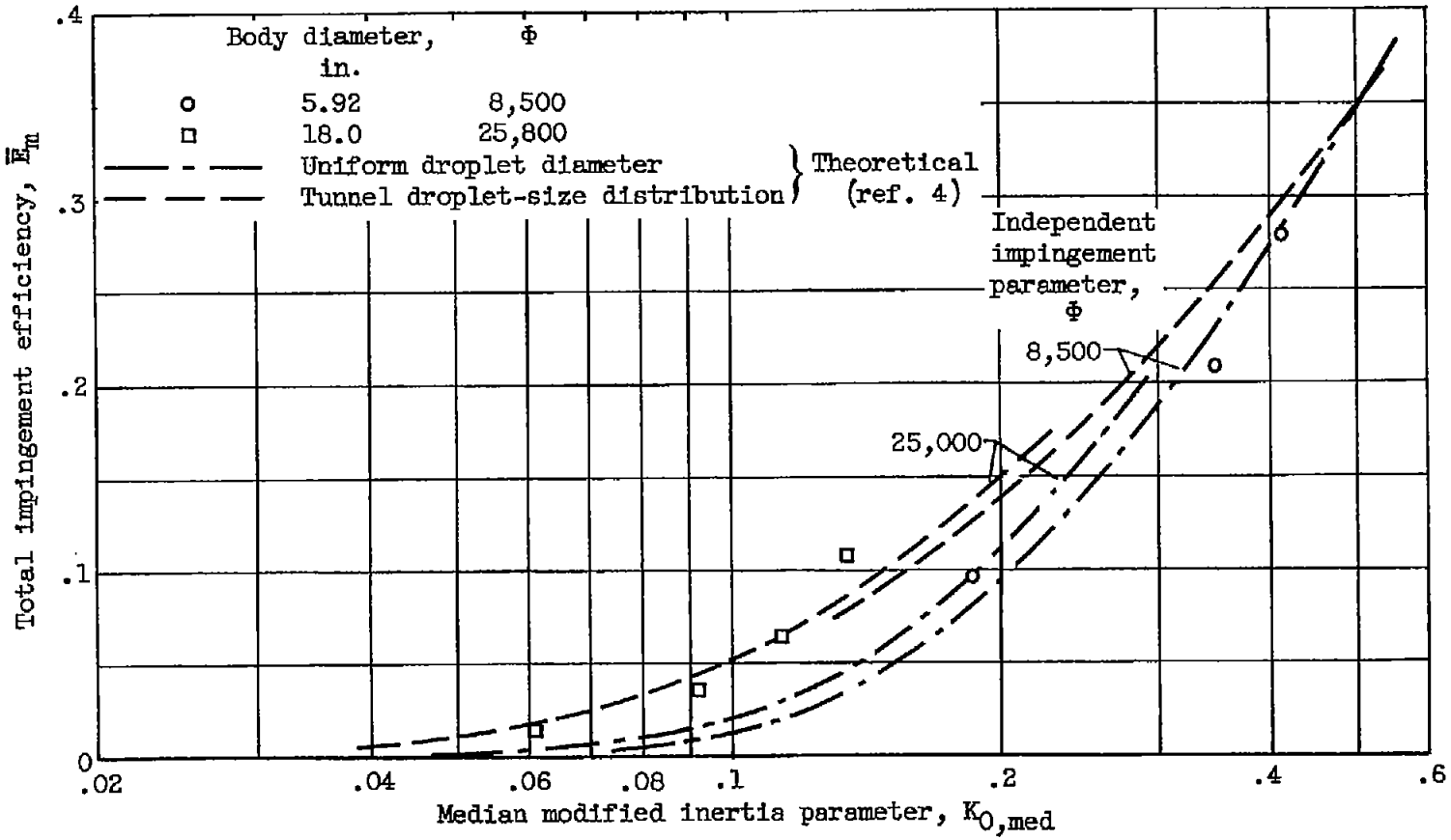

Figure 20. - Correlation of total impingement efficiency for spheres with modified inertia parameter.

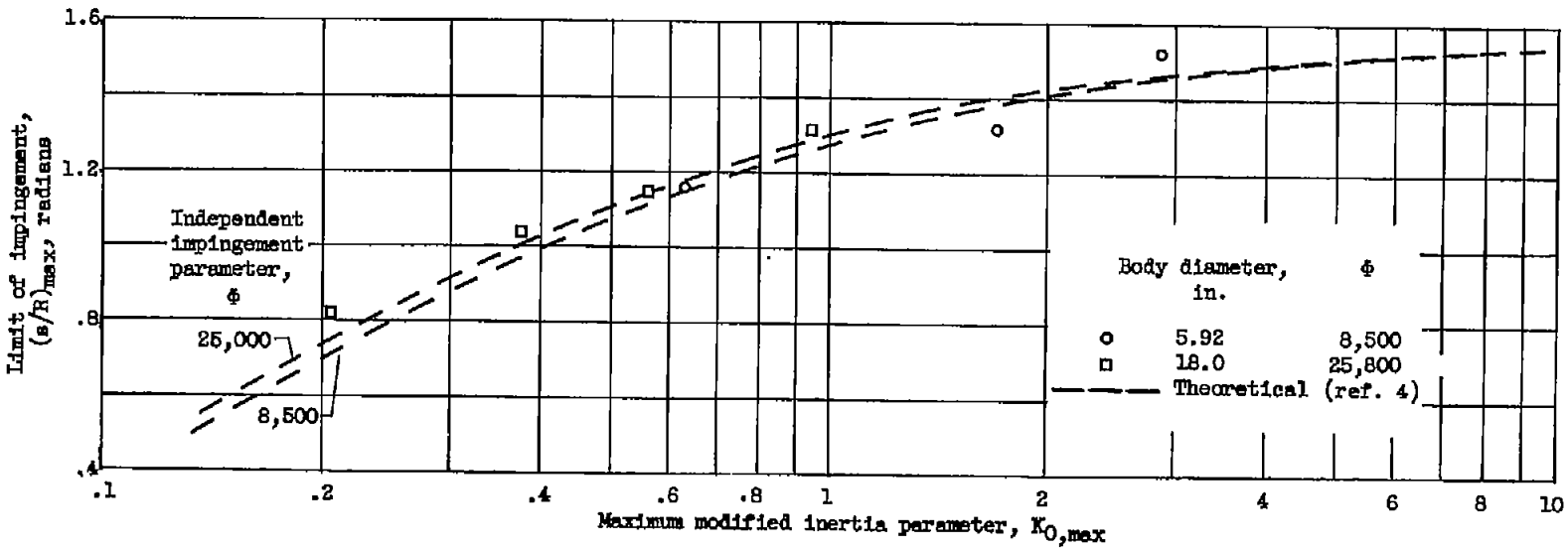

Figure 21. - Correlation of limit of impingement on spheres with modified inertia parameter.

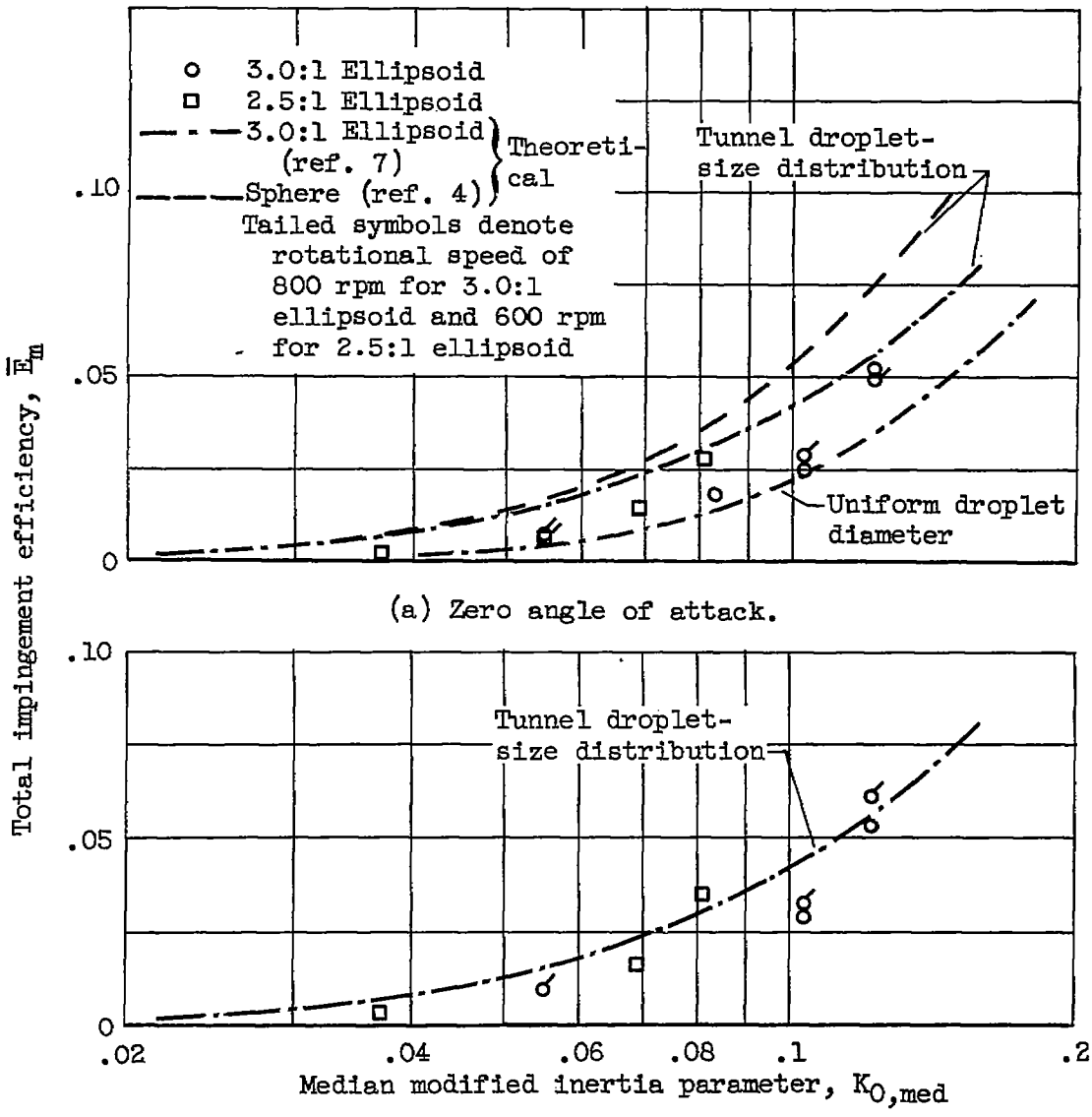

Figure 22. - Correlation of total impingement efficiency with modified inertia parameter for two ellipsoidal bodies at several operating and droplet-size conditions.

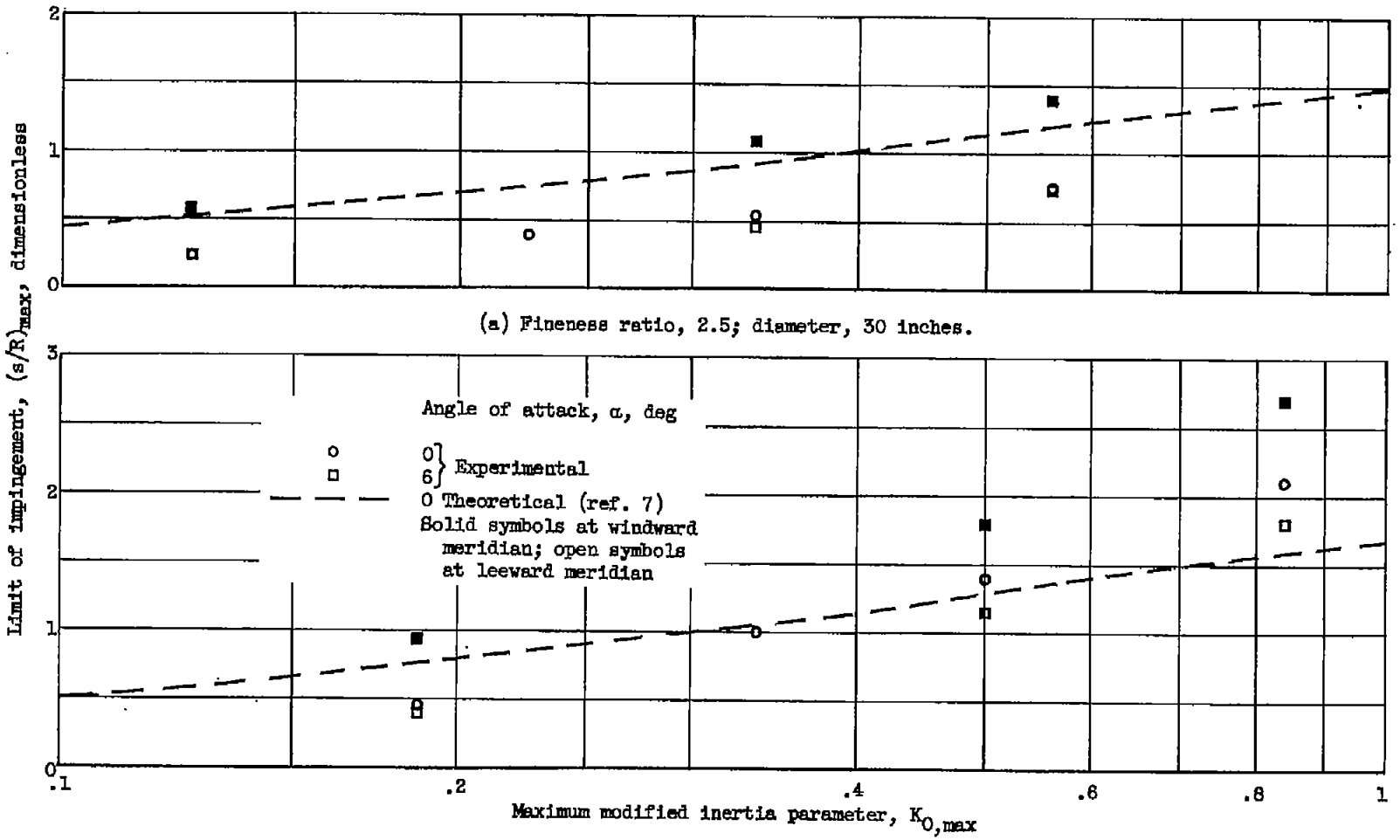

(a) Fineness ratio, 2.5; diameter, 30 inches.

(b) Fineness ratio, 3.0; diameter, 20 inches.

Figure 23. - Correlation of limit of impingement on two ellipsoids with modified inertia parameter at two angles of attack.

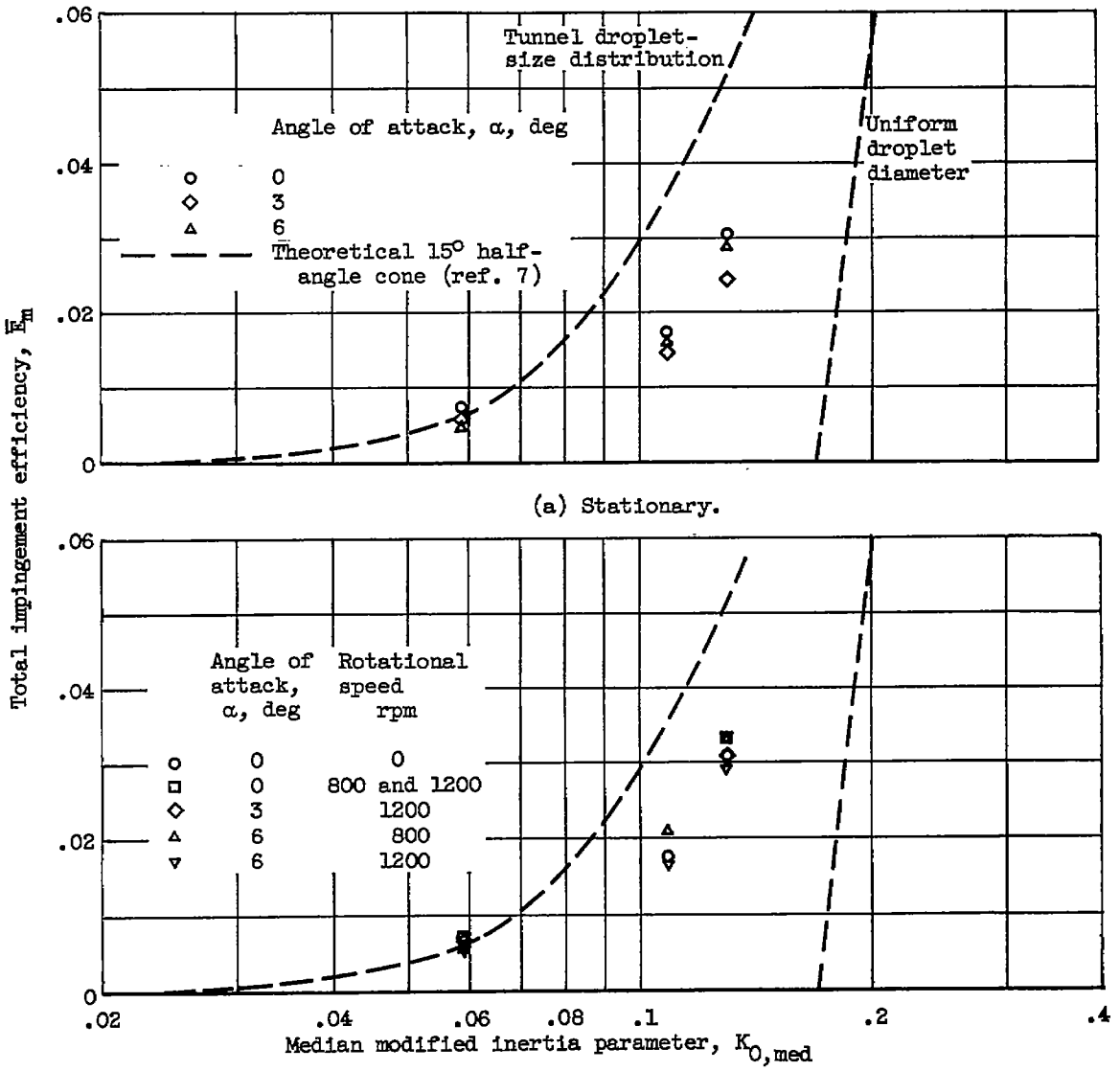

Figure 24. - Correlation of total impingement efficiency on conical forebody with modified inertia parameter.

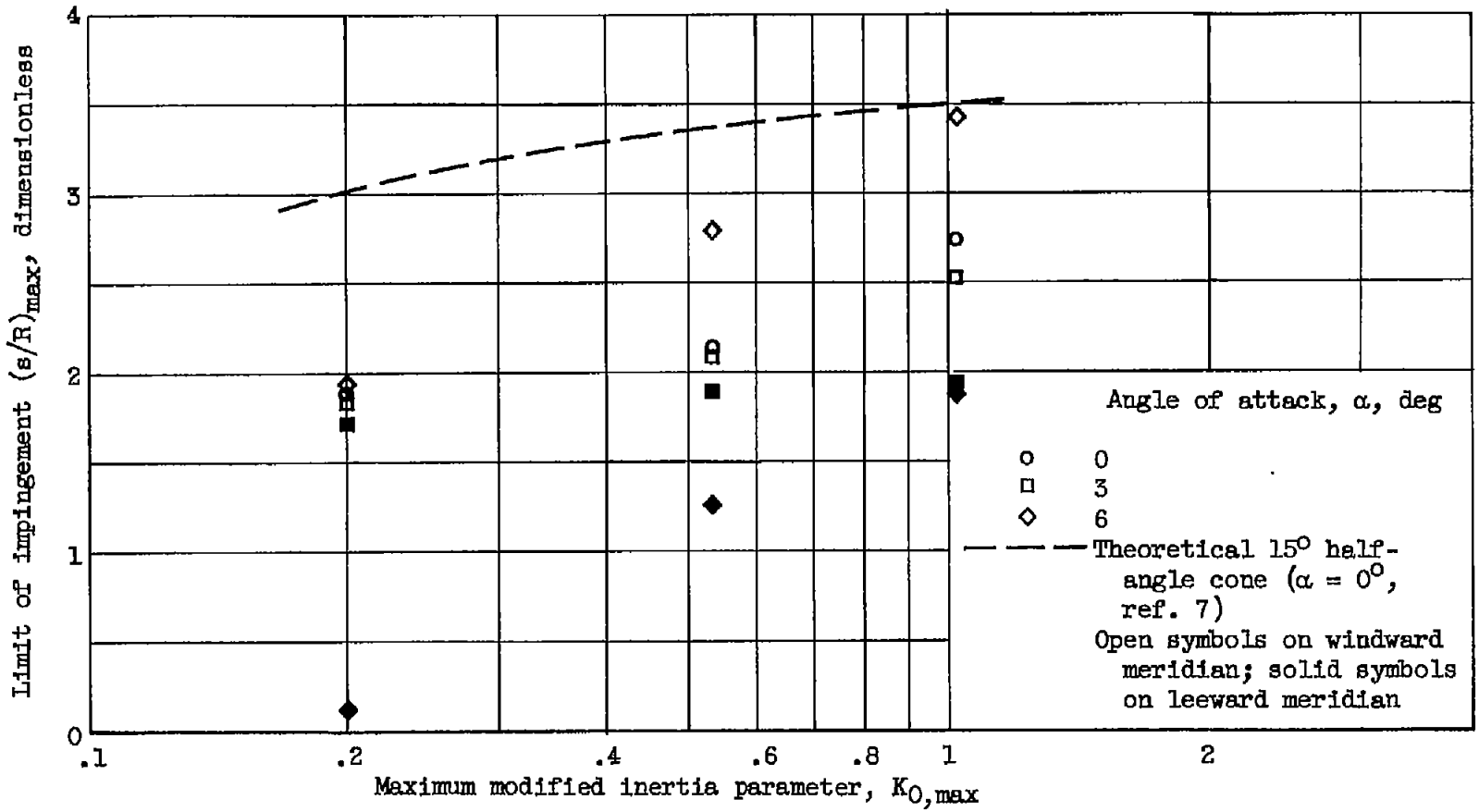

Figure 25. - Correlation of limit of impingement on conical forebody with modified inertia parameter.

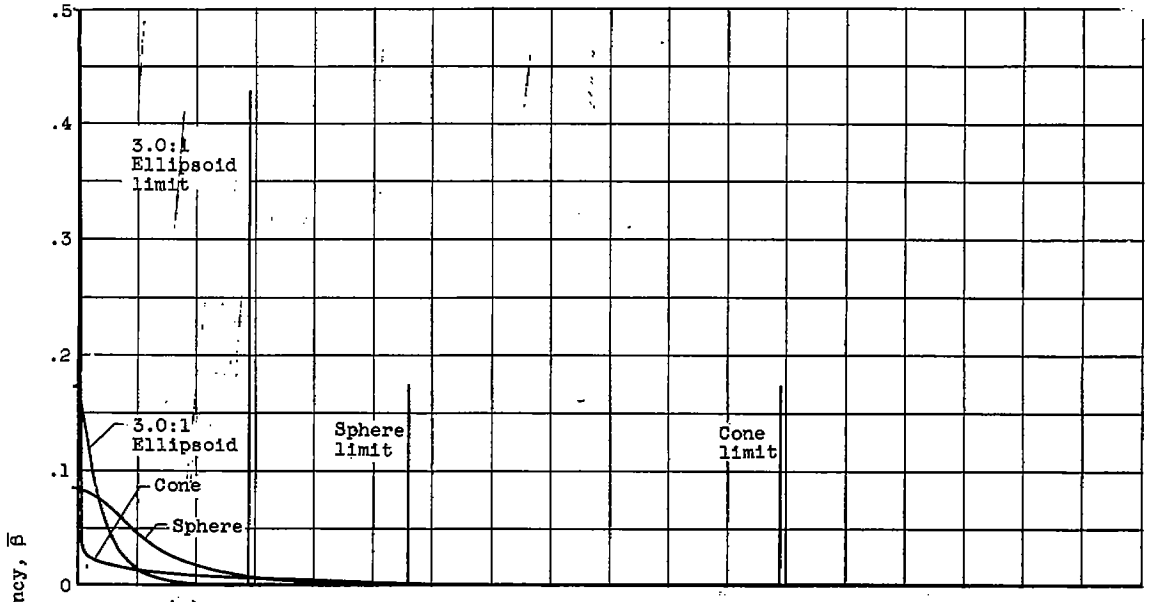

(a) Median modified inertia parameter, 0.06.

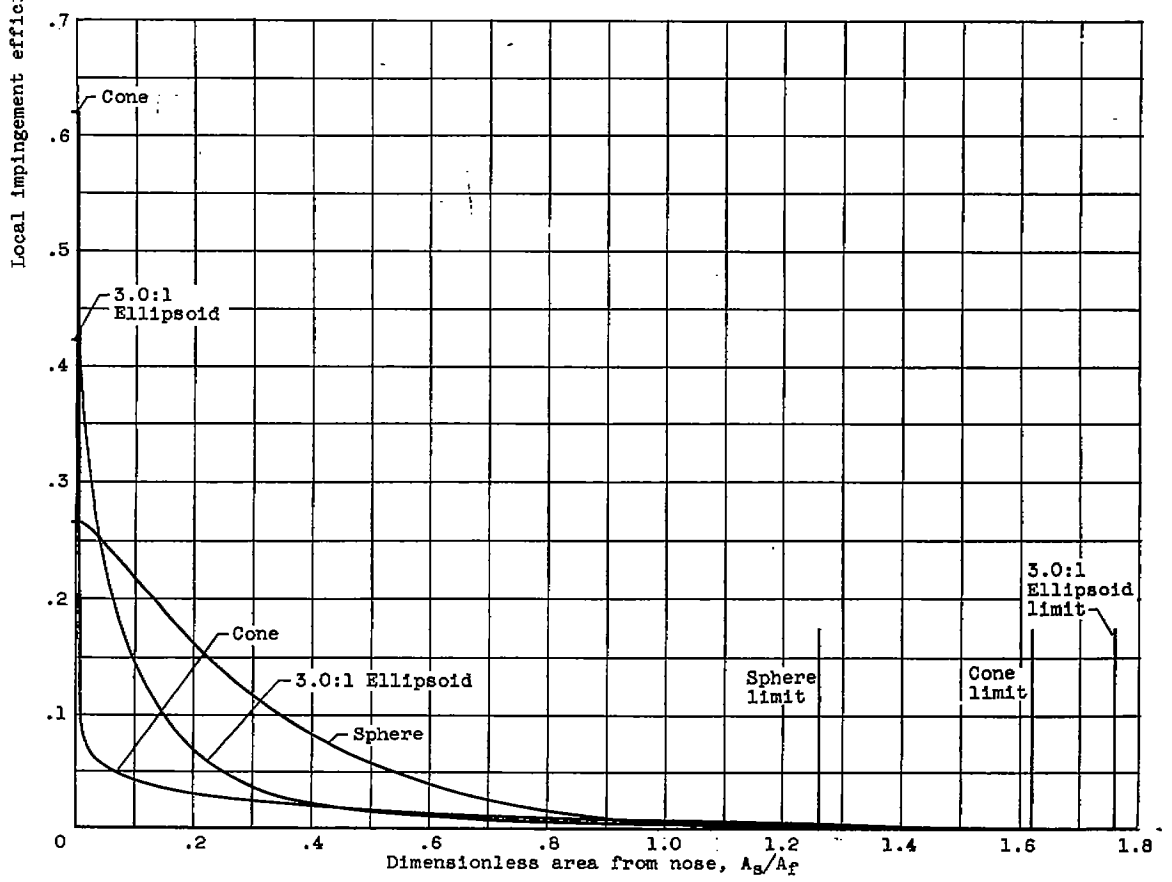

(b) Median modified inertia parameter, 0.12.

Figure 26. - Effect of body shape on local impingement efficiency for three stationary bodies of revolution at zero angle of attack.

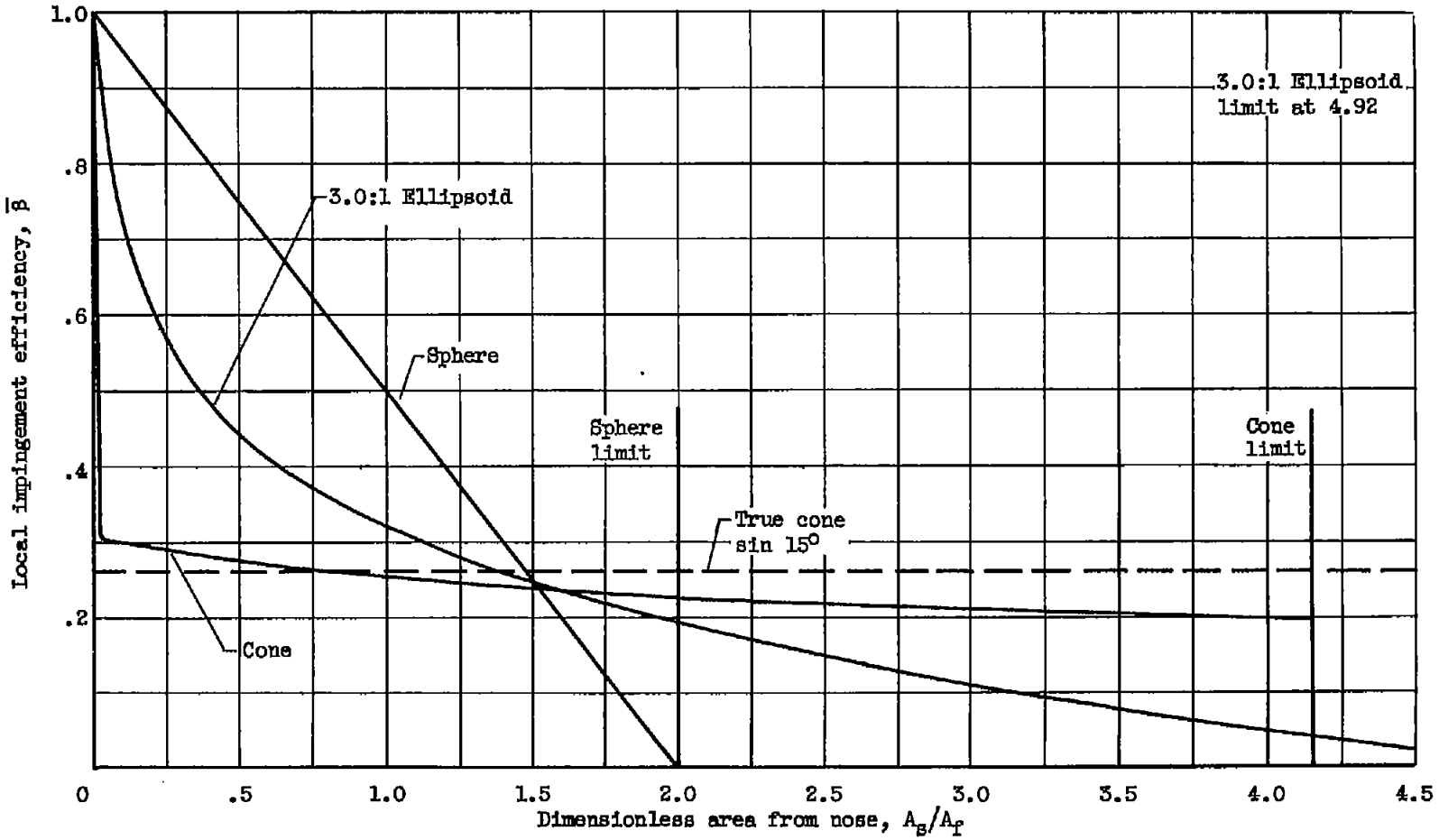

(c) Inertia parameter = ∞.

Figure 26. - Concluded. Effect of body shape on local impingement efficiency for three stationary bodies of revolution at zero angle of attack.